



저작자표시-비영리-변경금지 2.0 대한민국

이용자는 아래의 조건을 따르는 경우에 한하여 자유롭게

- 이 저작물을 복제, 배포, 전송, 전시, 공연 및 방송할 수 있습니다.

다음과 같은 조건을 따라야 합니다:



저작자표시. 귀하는 원저작자를 표시하여야 합니다.



비영리. 귀하는 이 저작물을 영리 목적으로 이용할 수 없습니다.



변경금지. 귀하는 이 저작물을 개작, 변형 또는 가공할 수 없습니다.

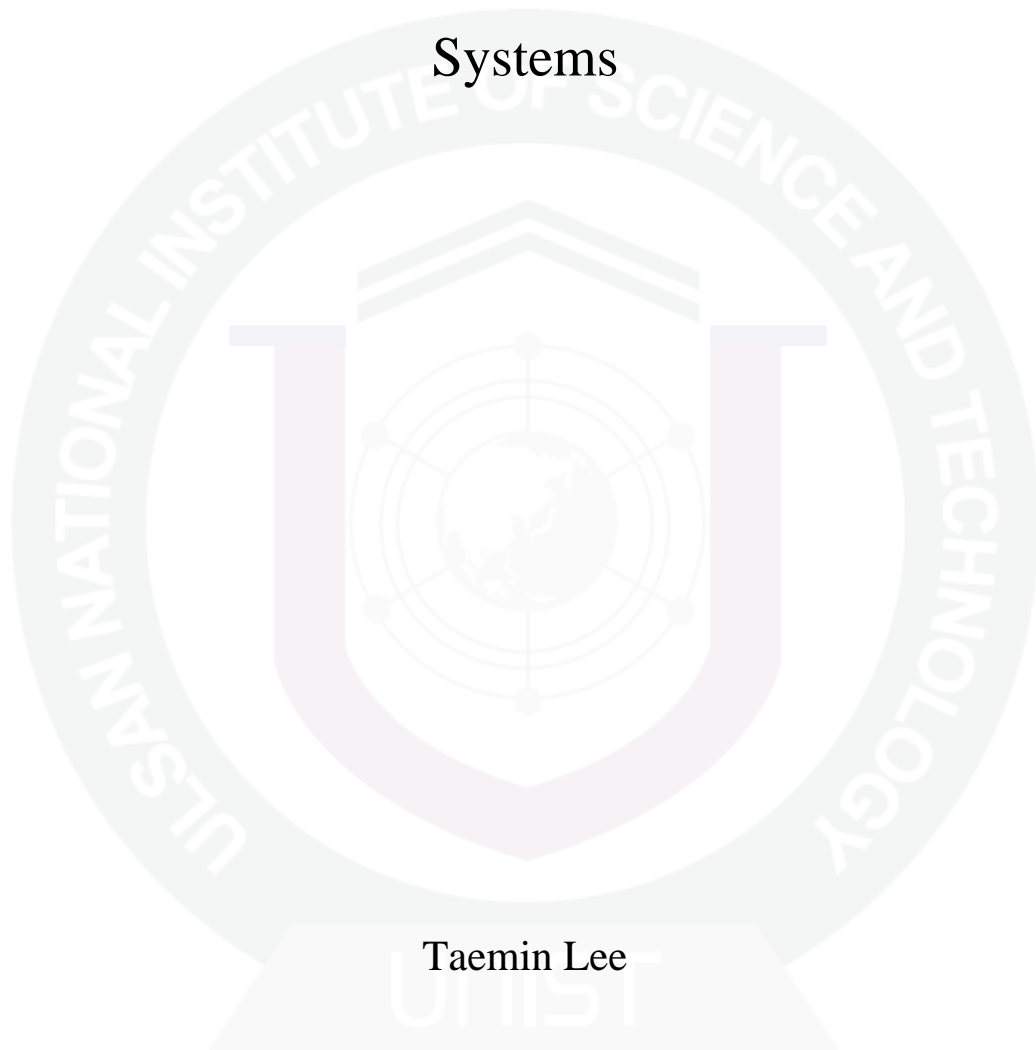
- 귀하는, 이 저작물의 재이용이나 배포의 경우, 이 저작물에 적용된 이용허락조건을 명확하게 나타내어야 합니다.
- 저작권자로부터 별도의 허가를 받으면 이러한 조건들은 적용되지 않습니다.

저작권법에 따른 이용자의 권리는 위의 내용에 의하여 영향을 받지 않습니다.

이것은 [이용허락규약\(Legal Code\)](#)을 이해하기 쉽게 요약한 것입니다.

[Disclaimer](#)

Chemically Modified Graphene Nanosheets
for Highly Efficient Energy Storage and Conversion
Systems



Taemin Lee

Nanochemistry

School of Nano-Bioscience and Chemical Engineering

Graduate School of UNIST

2013

Chemically Modified Graphene Nanosheets
for Highly Efficient Energy Storage and Conversion
Systems

Taemin Lee

Nanochemistry

School of Nano-Bioscience and Chemical Engineering

Graduate School of UNIST

Chemically Modified Graphene Nanosheets for Highly Efficient Energy Storage and Conversion Systems

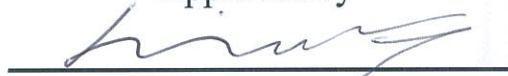
A thesis

submitted to School of Nano-Bioscience and Chemical Engineering
and the Graduate School of UNIST
in partial fulfillment of the
requirements for the degree of
Master of Science

Taemin Lee

02. 06. 2013 Month/Day/Year of submission

Approved by



Major Advisor

Byeong-Su Kim

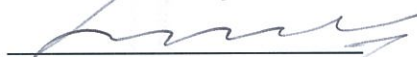
Chemically Modified Graphene Nanosheets For Highly Efficient Energy Storage and Conversion Systems

Taemin Lee

This certifies that the thesis of Taemin Lee is approved.

02. 06. 2013 Month/Day/Year of submission

[signature]



Thesis supervisor: Byeong-Su Kim

[signature]



Joon Hak Oh

[signature]



Tae-Hyuk Kwon

Contents

| | |
|--|----|
| Abstract..... | 1 |
| List of Figures and Tables..... | 2 |
| PART I. Hybrid Multilayer Thin Film Supercapacitor of Graphene Nanosheets with Polyaniline: Importance of Establishing Intimate Electronic Contact through Nanoscale Blending | |
| I. Introduction..... | 7 |
| 1.1 Basics of electrochemical energy storage systems..... | 7 |
| 1.2 Charge storage mechanisms of supercapacitor..... | 8 |
| 1.3 Graphene as an electroactive material for supercapacitor..... | 10 |
| 1.3.1 Graphene as a promising material for energy storage devices..... | 11 |
| 1.3.2 Various approaches for production of graphene nanosheets..... | 11 |
| 1.4 Hybrid nanomaterials for supercapacitor..... | 14 |
| 1.5 Fabrication of hybrid electrodes by Layer-by-Layer (LbL) Assembly..... | 14 |
| II. Experiments..... | 17 |
| 2.1 Preparation of polyaniline (PANi) suspension..... | 17 |
| 2.2 Preparation of graphene oxide (GO) suspension..... | 17 |
| 2.3 Fabrication of layer-by-layer assembled (PANi/GO) _n multilayer films..... | 17 |
| 2.4 Fabrication of electropolymerized PANi electrode..... | 17 |
| 2.5 Preparation of electrodes and electrochemical measurements..... | 18 |
| 2.6 Other characterization methods..... | 18 |
| III. Results and Discussion..... | 20 |
| 3.1 Layer-by-Layer assembly for hybrid PANi/GO electrodes..... | 20 |
| 3.2 Post-reduction treatments on hybrid PANi/GO electrodes..... | 21 |
| 3.3 Characterization of the structural and chemical properties of hybrid PANi/GO electrodes..... | 21 |
| 3.4 Electrochemical performance of hybrid PANi/GO electrodes for supercapacitor..... | 28 |
| IV. Conclusion..... | 35 |
| V. Reference..... | 36 |

PART II. Ionic Liquid Modified Graphene Nanosheets Anchoring Manganese Oxide Nanoparticles as Efficient Electrocatalysts for Zn-air Batteries

| | |
|--|----|
| I. Introduction..... | 42 |
| 1.1 Introduction of Zn-air battery..... | 42 |
| 1.2 Catalytic materials for air-electrode..... | 47 |

| | |
|---|----|
| 1.3 Exploration the ORR kinetics of catalysts based on the Koutecky-Levich equation..... | 48 |
| II. Experiments..... | 50 |
| 2.1 Procedures of graphene oxide (GO) nanosheets..... | 50 |
| 2.2 Preparation of ionic liquid moiety (IL-NH ₂)..... | 50 |
| 2.3 Preparation of ionic liquid modified graphene oxide nanosheet (GO-IL) and reduced graphene oxide nanosheets (rGO-IL)..... | 50 |
| 2.4 Preparation of catalyst ink for rotating disk electrode..... | 50 |
| 2.5 Rotating disk electrode (RDE) experiments..... | 50 |
| 2.6 Preparation of air electrode..... | 51 |
| 2.7 Zinc air full cell assembly..... | 51 |
| III. Results and Discussion..... | 52 |
| 3.1 Ionic liquid (IL) modified graphene nanosheets..... | 52 |
| 3.2 rGO-IL/Mn ₃ O ₄ nanocomposites for electrocatalysts..... | 52 |
| 3.3 Characterizations of rGO-IL/Mn ₃ O ₄ nanocomposites electrocatalysts..... | 52 |
| 3.4 Electrocatalytic activities of hybrid catalysts..... | 53 |
| 3.5 Zinc-air cell performance..... | 60 |
| IV. Conclusion..... | 65 |
| V. Reference..... | 66 |
| VI. Acknowledgements..... | 69 |

Abstract

Due to the resource exhaustion and environmental issues, the increasing energy demands have stimulated intense research on alternative energy storage and conversion systems with high efficiency, low cost, and environmental benignity. Graphene, two-dimensional sp^2 -hybridized carbon structure, has recently attracted enormous interest for promising electrode materials due to its superior properties such as high electrical conductivity, large surface area, and chemical and mechanical stability. Chemical exfoliation method has been the most popular protocols to achieving stable suspensions in various solvents. This approach is a very efficient and scalable; however, it unavoidably introduces the surface defects, which hamper the conductivity of the resulting graphene sheets. Nevertheless, chemically exfoliated graphene nanosheet provides an ideal single-atom-thick substrate for growth of functional nanomaterials to render them electrochemically active and electrically conductive properties due to many oxygen functional groups on the surface of graphene nanosheets. In addition, it can readily adding the other groups to graphene oxide nanosheets using various chemical reactions that provides for either covalent or non-covalent attachment to the resulting chemically modified graphenes. Such approaches, which add functionality to groups that are already present on the graphene oxide, render graphene oxide a more versatile precursor for a wide range of applications.

In this study, we synthesized diverse graphene-based nanocomposites by chemical functionalization and demonstrated for energy storage and conversion systems with enhanced electrochemical performance.

List of Figures

Figure 1. Specific power against specific energy, also called a Ragone plot, for various electrical energy storage devices. If a supercapacitor is used in an electric vehicle, the specific power shows how fast one can go, and the specific energy shows how far one can go on a single charge. Times shown are the time constants of the devices, obtained by dividing the energy density by the power.

Figure 2. Mother of all graphitic forms. Graphene is a 2D building material for carbon materials of all other dimensions. It can be wrapped up into 0D buckyballs, rolled into 1D nanotubes or stacked into 3D graphite.

Figure 3. Various approaches for synthesis of graphene (a) Chemical vapor deposition (CVD), epitaxial growth, and micromechanical exfoliation. (b) Chemical route to the synthesis of aqueous graphene dispersions. (1) Oxidation of graphite to graphite oxide with greater interlayer distance. (2) Exfoliation of graphite oxide in water by sonication to obtain GO colloids that are stabilized by electrostatic repulsion. (3) Controlled conversion of GO colloids to conducting graphene colloids through deoxygenation by hydrazine reduction

Figure 4 (a) Schematic illustration of the layer-by-layer (LbL) assembled multilayer film deposition process based on electrostatic interaction and a simplified multilayer film built up from a negatively charged substrate. (b) A schematic illustration of the multilayer film deposition process based on the dipping, spraying, and consecutive spinning process of anionic and cationic polyelectrolytes.

Figure 5. (a) UV/vis spectra and (b) ellipsometry thickness of as-assembled (PANi/GO)_n multilayer films as a function of the number of bilayers. The number on each graph represents the number of bilayer (*n*). Inset in Fig 5a is the image of corresponding samples from 2- to 10-bilayer. Thickness is the average values of five independent measurements. (c) Plot of the UV/vis absorption peak at 319 nm of PG_n multilayer film as a function of the number of bilayers constructed with varying pH of GO suspension at a fixed pH of PANi (pH 2.5). (d) Representative photograph image of LbL-assembled hybrid electrodes of (left) PG₁₀ (middle) PG₁₀-H, and (right) PG₁₀-HC.

Figure 6. Representative images of as-assembled PG₂₀ multilayer films: (a) SEM and (b,c) TEM with a corresponding elemental mapping. Inset in (a) shows the surface morphology. (d-f) Height-mode AFM images of (d) as-assembled PG₁₀, (e) heat treated PG₁₀-H, and (f) both heat- and chemical-treated PG₁₀-HC.

Figure 7. High-resolution (a) C1s and (b) N1s XPS spectra of all (PANi/GO)₁₀ multilayer films with and without post-treatments. The percentage under the sp² label in Fig 7a represents the fraction of sp²-carbon.

Figure 8. (Top) Cyclic voltammogram (CV) curves of all (PANi/GO)_n hybrid electrode films with various scan rates from 10 to 200 mV/s. (a) As-prepared PG₁₀, (b) heat-treated PG₁₀-H, (c) heat- and chemically-treated PG₁₀-HC, and (d) heat-treated (GO/GO)₁₀. All electrochemical properties were collected in a three-electrode system with a Ag/AgCl reference in 1.0 M H₂SO₄ electrolyte at identical scan rates presented in (d). Note that the y-scale in (d) is significantly smaller than the others. (Bottom) Plot of the peak current density (mA/cm²) vs potential scan rate (mV/s) of PG₁₀-H in an equi-span log-log scale. The slopes were estimated to be around 1.0 for both cases.

Figure 9. Galvanostat charge/discharge curves of the assembled hybrid (PANi/GO)₁₀ electrodes. (a) PG₁₀, (b) PG₁₀-H, and (c) specific capacitance values as a function of discharge current density from 0.5 to 3 A/g. (d) Comparison of cycling stability of all samples at a high discharge current density of 3 A/g. Electropolymerized pure PANi film was used for comparison.

Figure 10. Ragone plot of the LbL-assembled hybrid PG₁₀ (black-line) and PG₁₀-H (red-line) supercapacitor electrodes measured at different discharge current density from 0.5 to 3 A/g.

Figure 11. Comparison of the gravimetric energy density of some representative types of primary/rechargeable batteries, metal–air batteries, H₂–air fuel cell and gasoline. The theoretical values are calculated on the basis of thermodynamics of active materials.

Figure 12. Schematic representation of the structure and operation principle of a metal-air battery.

Figure 13. Working principle and each electrode reaction of zinc-air battery. Note the red circle where three phase reaction (oxygen (gas)–catalysts (solid)–electrolyte (liquid)) occur in air cathode.

Figure 14. Trends in oxygen reduction activity (defined in the text) plotted as a function of the oxygen binding energy.

Figure 15. Deconvoluted high-resolution N1s XPS spectra of samples in this study. (a) GO, (b) rGO-IL, and (c) rGO-IL/Mn₃O₄ (10:1).

Figure 16. X-ray diffraction pattern of prepared hybrid rGO-IL/Mn₃O₄ (2:1) with the reference Mn₃O₄

diffraction pattern.

Figure 17. (a) SEM and (b) TEM images of rGO-IL/Mn₃O₄ composites with size-distribution of Mn₃O₄ nanoparticles. (c) HR-TEM image of Mn₃O₄ nanoparticles with the inset of the corresponding SAED pattern and (d, e, f) STEM and the EDX elemental mapping image of hybrid rGO-IL/Mn₃O₄ (10:1) composites.

Figure 18. Rotating disk electrode (RDE) experiments of various samples prepared in this study. (a) half-cell data and (b) comparison of onset potential and limiting current of each sample of GO, GO-IL, rGO-IL, rGO-IL/Mn₃O₄ (2:1), and rGO-IL/Mn₃O₄ (10:1). The rotation rate is 3200 rpm and the scan rate is 10 mV/s; 0.10 M KOH is used as an electrolyte. Pt wire and Hg/HgO is used as a counter and reference electrode with a 3-mm² diameter working electrode, respectively. Onset potential was measured at -0.002 mA/cm² and limiting current was measured at -0.45 V.

Figure 19. TGA thermograms of all samples used in this study. rGO-IL/Mn₃O₄ (2:1) and rGO-IL/Mn₃O₄ (10:1) show the relative percentage of Mn₃O₄ within the composite is 52.5% and 19.2%, respectively. The thermograms were obtained at a scan rate of 10 °C/min under air.

Figure 20. RDE experiments and the corresponding Koutecky-Levich plots of (a, b) rGO-IL/ Mn₃O₄ (2:1) and (c, d) rGO-IL/Mn₃O₄ (10:1). The experiments were conducted at a scan rate of 10 mV/s in an O₂-saturated 0.10 M KOH solution. Theoretical slopes for $n = 2$ and 4 are also constructed for comparison.

Figure 21. Schematic representation of the potential pathway of electrons during oxygen reduction reaction on the surface of rGO-IL/Mn₃O₄ electrocatalysts.

Figure 22. Single cell performance of zinc air battery assembled with hybrid rGO-IL/Mn₃O₄ electrocatalysts. (a) Polarization curve of zinc-air cell and (b) corresponding power density plot of (black) rGO-IL/Mn₃O₄ (2:1) and (red) rGO-IL/Mn₃O₄ (10:1) under the current density from 0 to 200 mA/cm².

List of Schemes

Scheme 1. Schematic representation of layer-by-layer (LbL) assembled multilayer thin film of PANi with graphene oxide nanosheets with a photograph of the film assembled on a flexible PET substrate.

Scheme 2. (a) Schematic representation of the functionalization of the surface of graphene oxide and subsequent formation of nanoparticles. (b) Cartoon of Zn-air battery cell with a photograph of the actual cell tested.

List of Tables

Table 1. XPS peak assignments of deconvoluted C 1s and N 1s composition with relative percentage of each peak.

Table 2 Specific capacitance values of hybrid PG₁₀, PG₁₀-H, PG₁₀-HC, and GG₁₀-H electrodes obtained from cyclic voltammograms and galvanostat charge/discharge experiments.

PART I. Hybrid Multilayer Thin Film Supercapacitor of Graphene Nanosheets with Polyaniline: Importance of Establishing Intimate Electronic Contact through Nanoscale Blending

I. INTRODUCTION

A global energy issue on the environmental pollution and depletion of fossil fuels is one of the major challenges that our society faces in recent days. In addition, the increasing energy demands for portable devices and hybrid electric vehicles have stimulated intense research on sustainable and renewable energy sources with high efficiency, low cost, and environmental benignity.¹⁻³ To satisfy the high requirements for emerging systems, electrochemical energy storage and conversion systems such as rechargeable batteries, fuel cells, and supercapacitors, have been widely studied to alternate the fossil fuels. Among these electrochemical devices, supercapacitors, also known as ultracapacitors or electrochemical capacitors (ECs), have received considerable attention as an attractive power source due to their complementary performance with respect to rechargeable batteries and fuel cells.^{2,4-9}

Thus, we present the development of hybrid supercapacitors with tailored compositions and architectures that combine the concept of an electric double-layer capacitor of graphene materials and a pseudocapacitor. More specifically, by taking advantage of LbL assembly, we constructed a hybrid supercapacitor consisting of a graphene oxide (GO) nanosheet and a conducting polymer polyaniline (PANi) based on electrostatic interactions. Because LbL-assembled PANi with graphene nanosheets has not yet been fully explored, here we carefully investigated the dependence of the electrochemical performance of hybrid thin films on the various parameters of LbL assembly, such as the number of bilayers and the post-thermal and chemical treatments that could affect the degree of reduction in GO and PANi. We also demonstrated the redox state of PANi, is closely related to the stability and performance of the hybrid electrode.

1.1 Basics of electrochemical energy storage systems

As illustrated in **Figure 1**, where energy conversion and storage devices are compared and presented in the simplified ‘Ragone plot’.^{8,10} The electrochemical performance of an energy storage device is determined by two key parameters, one is energy density (E) that means the amount of energy stored per unit mass and can be expressed by the equation:

$$E = \frac{1}{2} CV^2$$

where C is the specific capacitance, and V is the voltage. The other factor is power density (P) which is the amount of energy delivered per unit mass and can be expressed by the equation:

$$P_{max} = \frac{1}{4R_s} V_i^2$$

where R_s is the equivalent series resistance (ESR) and V_i is the initial voltage. Through the Ragone plot, we can note that the conventional rechargeable batteries and fuel cells provide a high energy density, but with a low power density. Meanwhile, even though the conventional capacitors possess a high power density, they cannot offer a high energy density to meet requirement for long duration applications.

Conventional capacitors, which consisting of two conducting electrodes separated by an insulating dielectric material, store the energy by electrostatically positive and negative charges on the surface of each electrodes.⁵ They exhibit a prominent feature of fast charge/discharge rate in a few second; as a consequence, a much high power delivery or uptake (10 kW/kg) can be achieved for a short time. However, its energy density (about 5 Wh/kg) is relatively low compared with other energy storage systems. Rechargeable batteries and fuel cells can store the charges by chemical redox reaction between active materials and electrolyte ions, which leads to high energy density.¹¹⁻¹³ Despite their relatively high specific energies, batteries still suffer from severe drawbacks; low charge-discharge rates and a sluggish power delivery or uptake.

Supercapacitor, which stores the energy by using either ion adsorption or fast surface redox reactions, the electrochemical behavior placed somewhere between the conventional capacitors and batteries. It can store hundreds or thousands of times more charges than that of conventional capacitor due to a large specific surface area (SSA), while it can charge and discharge quickly in few minutes like a conventional capacitor. In addition, it delivers high levels of electrical power and offers long operating lifetime, which employs an important role for emergency or back-up power supplies to protect against power disruption.¹⁴ However, a major weakness of supercapacitor is its relatively low energy density (typically 5–10 Wh/kg), which is significantly lower than the lead-acid (20–35 Wh/kg), Ni metal hydride (40–100 Wh/kg), and lithium-ion batteries (120–170 Wh/kg). Despite their low energy density, a number of distinctive features such as high power density, fast charge–discharge capability, long cycle life, wide thermal operating range, and low maintenance cost clearly provide supercapacitors high potential as energy storage devices.^{1, 15, 16} Thus, supercapacitor offers promising approach to meet the increasing power demands of energy storage devices together with synergistic benefits both from the capacitor and battery properties.

1.2 Charge storage mechanisms of supercapacitor

Supercapacitors can be categorized by electric double-layer capacitors (EDLCs) and pseudocapacitors depending on the charge storage mechanisms and the type of active electrode materials.⁵ The most common EDLCs devices, use carbon-based active materials with high surface

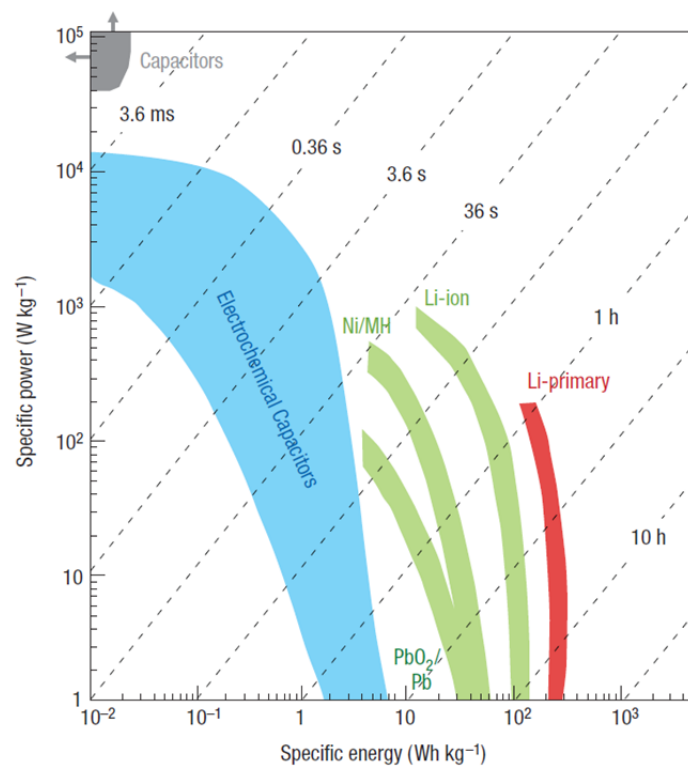


Figure 1. Specific power against specific energy, also called a Ragone plot, for various electrical energy storage devices. If a supercapacitor is used in an electric vehicle, the specific power shows how fast one can go, and the specific energy shows how far one can go on a single charge. Times shown are the time constants of the devices, obtained by dividing the energy density by the power.⁸

area, and the capacitance comes from the electrostatic charge accumulation on the electrode/electrolyte interface. The concept of the EDLCs was first described by Helmholtz in 1853, when he investigated the distribution of alternative charges at the interface of colloidal particles.¹⁷ The Helmholtz double layer model is similar to that of two conducting electrode conventional capacitors. This capacitance model was later refined by Gouy and Chapman, and Stern and Geary, who suggested the presence of a diffuse layer in the electrolyte due to the accumulation of ions near the surface of electrode.¹⁸⁻²⁰ The diffuse layer was formed by a continuous distribution of electrolyte ions (both cations and anions) in the electrolyte solution, indicating that the specific capacitance is highly dependent on the type of electrolyte ions and chemical affinity between the adsorbed ions and electrode surface. For example, specific capacitance of EDLCs achieved with aqueous alkaline or acid solutions is generally higher than inorganic electrolytes.²¹ Moreover, it has no limitation by the electrochemical kinetics through a polarization resistance and allows very fast energy delivery and uptake, and better power performance. However, as a consequence of the electrostatic surface charging mechanism, these devices suffer from a relatively low energy density, which is not enough to alternate the secondary batteries.

In contrast, the pseudo- or redox- capacitors store the charges by the fast-reversible chemical redox reactions between electrolyte and electroactive species on the electrode surface, like conventional batteries. The metal oxides (*e.g.* RuO₂, Fe₃O₄, and MnO₂)²²⁻²⁶ as well as electrically conducting polymers (*e.g.* polyaniline and polypyrrole),^{27, 28} have been extensively studied as electroactive materials. The specific capacitance value of pseudocapacitive materials exceeds that of carbon materials based EDLCs, but they often suffer from a lack of stability during charge/discharge cycling, like batteries, due to the instability of materials during fast redox reactions.

1.3 Graphene as an electroactive material for supercapacitor

Carbon-based materials ranging from activated carbons to carbon nanotubes (CNTs) are the most widely used electrode materials because of their unique and characteristic physical and chemical properties. These properties include low cost, variety of form (powders, fibers, aerogels, composites, sheets, monoliths, tubes, etc.), ease of processability, relatively inert electrochemistry, controllable porosity and electrocatalytic active sites for a variety of redox reactions.^{21, 29} In the development of EDLCs, a proper control over the specific surface area and the pore size adapted to an appropriate type of electrolyte solution is crucial to ensure a good performance of the supercapacitor in terms of both power delivery rate and energy storage capacity.

Activated carbons are often considered as EDLC electrode materials because of their high surface area and controllable pore size, depending on the method of activation (chemical or physical activation). Templated porous carbons of microporous, mesoporous and macroporous sizes with a tailorable hierarchical structure hold a great promise as supercapacitor electrode materials.³⁰ In

addition, CNTs are of particular interest for the development of supercapacitor electrodes because of their unique tubular porous structures and superior electrical properties, which favor fast ion and electron transportation. More recently, the rise of graphene, which is a new class of two-dimensional carbon nanostructure, having large specific surface area and exceptionally high electronic properties, is forecasted to have a high potential in supercapacitor applications.

1.3.1 Graphene as a promising material for energy storage devices

Among many promising materials used for supercapacitors, carbon-based materials have been widely employed as electrode materials due to their excellent electrical conductivity and high surface area (**Figure 2**). In particular, graphene, a two-dimensional monolayer of an sp^2 -carbon network, has recently emerged as a novel nanomaterial that has stimulated intense research in the energy field of material science and technology due to its remarkable physicochemical properties.³¹⁻³⁶ It has a large theoretical specific surface area (2630 m^2/g),³⁷ high intrinsic mobility of charge carriers (200 000 $cm^2/V\cdot s$),³⁸ high Young's modulus (~ 1.0 TPa),³⁵ fracture strength (125 GPa),³⁵ and thermal conductivity (~ 5000 W/K·m),³⁹ and its optical transmittance ($\sim 97.7\%$ in visible region) and high electrical conductivity³⁸ merit attention for promising candidates as components in applications such as transparent conductive electrode,^{40, 41} 'paper-like' materials,^{42, 43} polymer composites,^{32, 44} and mechanical resonators.⁴⁵ Especially, its unique physicochemical properties suggest it has great potential for providing new approaches and critical improvements in the electrochemistry field of energy storage and conversion devices.³⁷

1.3.2 Various approaches for production of graphene nanosheets

Graphene has been prepared by following diverse methods (**Figure 3**). First, the micromechanical exfoliation, which is also known as the scotch tape or peel-off method, was first developed by Geim and Novoselov in 2004.^{31, 46} It is a very simple and facile method for producing the isolated graphene nanosheets from natural graphite without any degradation of their unique physical and chemical properties. Second is epitaxial growth on electrically insulating surfaces such as SiC.⁴⁷ Epitaxial growth of graphene nanosheets offers the advantage of structural coherence over large areas, because the azimuthal orientation of graphene is governed, to a large degree, by the crystal structure of the substrate surface. Third is chemical vapor deposition (CVD) such as the decomposition of gaseous ethylene or methane on metal substrates.^{36, 48} CVD method provides a production of highly qualified and electronic conductive graphene nanosheets with large lateral size. Finally, the chemical exfoliation method was widely studied to make homogeneous colloidal graphene oxide suspensions in aqueous or various organic solvents. Chemical exfoliations have been widely studied by the Brodie, Satudenmaier, and Hummers in the nineteenth century.⁴⁹⁻⁵¹ As recently demonstrated by Ruoff and co-workers,⁵² the solution-based route involves chemical oxidation of graphite to hydrophilic graphite

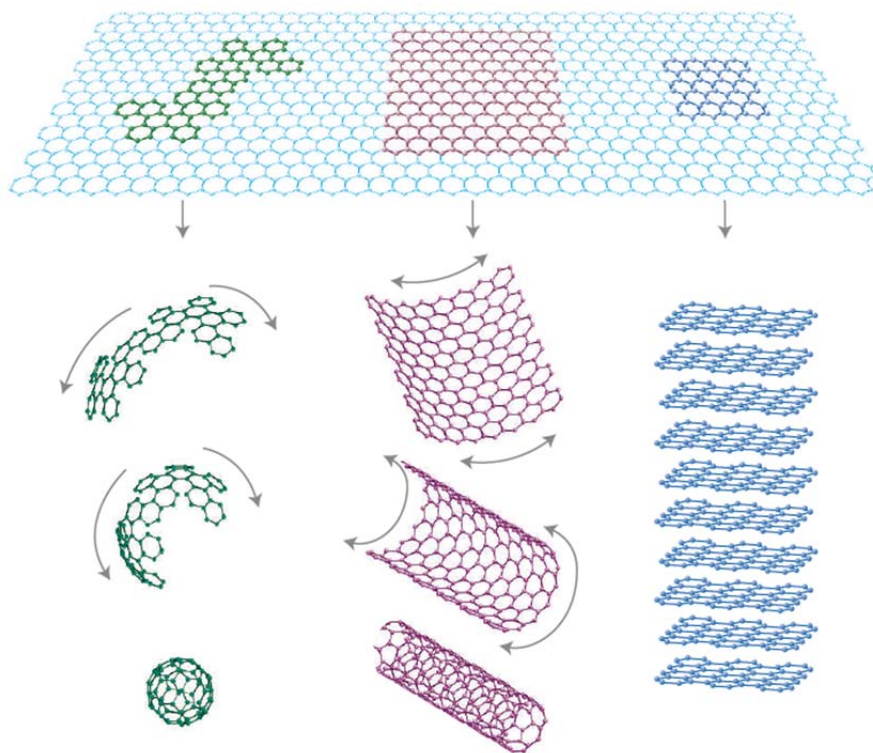


Figure 2. Mother of all graphitic forms. Graphene is a 2D building material for carbon materials of all other dimensions. It can be wrapped up into 0D buckyballs, rolled into 1D nanotubes or stacked into 3D graphite.³³

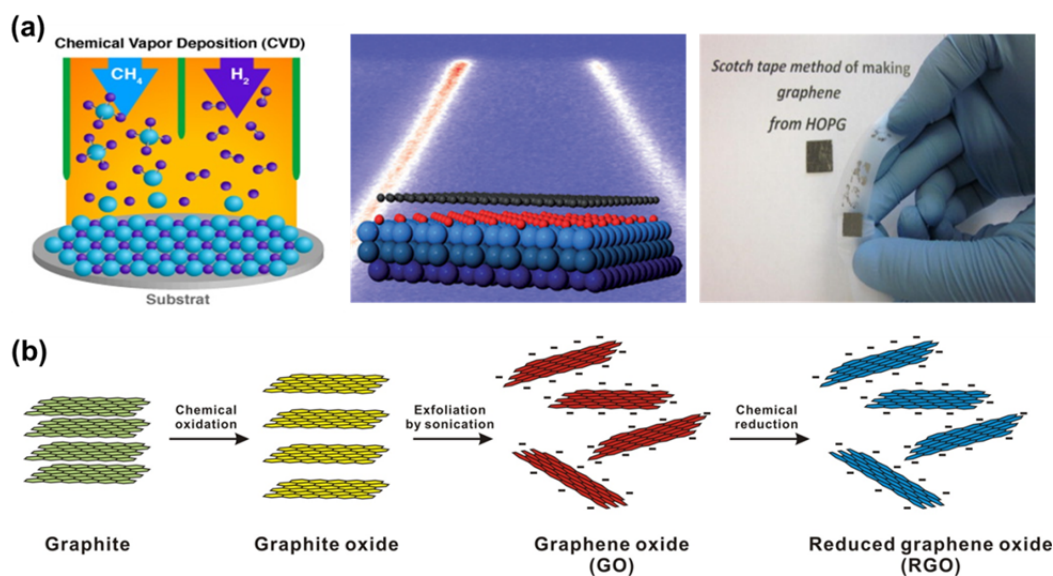


Figure 3. Various approaches for synthesis of graphene (a) Chemical vapor deposition (CVD), epitaxial growth, and micromechanical exfoliation. (b) Chemical route to the synthesis of aqueous graphene dispersions. (1) Oxidation of graphite to graphite oxide with greater interlayer distance. (2) Exfoliation of graphite oxide in water by sonication to obtain GO colloids that are stabilized by electrostatic repulsion. (3) Controlled conversion of GO colloids to conducting graphene colloids through deoxygenation by hydrazine reduction

oxide, which can be readily exfoliated as individual graphene oxide (GO) nanosheets by ultrasonication in water. Graphene oxide, which is electrically insulating, can be converted back to conducting graphene by chemical reduction. This approach involves chemical oxidation of graphite in the presence of strong acids and oxidants which not only readily change the degree of the oxidation on the basis of the method protocol, but also provides a promising route to achieve mass production. Moreover, the many oxygen functional groups on the surface of graphene nanosheets render them a good candidate for use in the various electrochemical energy storage fields through chemical functionalization.

1.4 Hybrid nanomaterials for supercapacitor

Despite these favorable features, the use of graphene and related carbon materials in supercapacitors is still limited due to their low capacitance (typically in the range of 10–10² F/g) and unsatisfactory performance to meet the high-power performance requirements. In order to overcome these limitations, there have been reports of preparing hybrid electrodes by combining graphene with other nanomaterials such as metal oxides and conducting polymers, thus providing the advantages of each component.⁵³⁻⁵⁸

Polyaniline (PANi), which is a conducting polymer, has been considered a promising material for energy storage and conversion with its excellent pseudocapacitive behavior, exhibiting a fast, reversible faradic reaction on the electrode surface, together with its high conductivity and ease of synthesis.⁵⁹ With these potential benefits, much promising research has been reported to date on combining graphene nanosheets with electrochemically active PANi, including simple solution mixing,^{60, 61} in situ polymerization,^{57, 62} and electropolymerization.^{63, 64}

Although these recent progresses present facile routes for the fabrication of hybrid electrode films of graphene, many of the resulting hybrid films suffer from a lack of precise control over the film architecture and properties, leading to a loss of the active surface area of the graphene sheets and intimate electrochemical interfaces necessary for maximum energy storage. Therefore, it continues to be a challenging endeavor to realize the nanoscale uniform blend of the hybrid structure of graphene nanosheets with other nanomaterials in a well-defined composition and structure.

1.5 Fabrication of hybrid electrodes by Layer-by-Layer (LbL) Assembly

The layer-by-layer (LbL) assembly, first introduced by Iler⁶⁵ and later by Decher,⁶⁶ is very simple and effective methods to make multifunctional hybrid architectures with nanometer-scale control (**Figure 4**). The LbL technique is not only applicable to polyelectrolyte-based systems, but also to almost any type of charged species, including inorganic molecular clusters, nanoparticles, nanotubes, nanoplates, micelles, block copolymers, polypeptides, DNA, and viruses. These materials can be successfully incorporated as components to create diverse functions with unique physical and

chemical properties by controlling structural differences. This approach generally occurred on the basis of the intermolecular electrostatic interactions, hydrogen bonding, covalent bonding, charge transfer interactions, host-guest interactions, and even biological recognition motifs. As a result, LbL assembly can be highly adaptable to assemble the nanoscale uniform blend of the hybrid structure of graphene nanosheets with other nanomaterials in a well-defined composition and structure.⁶⁶⁻⁷¹

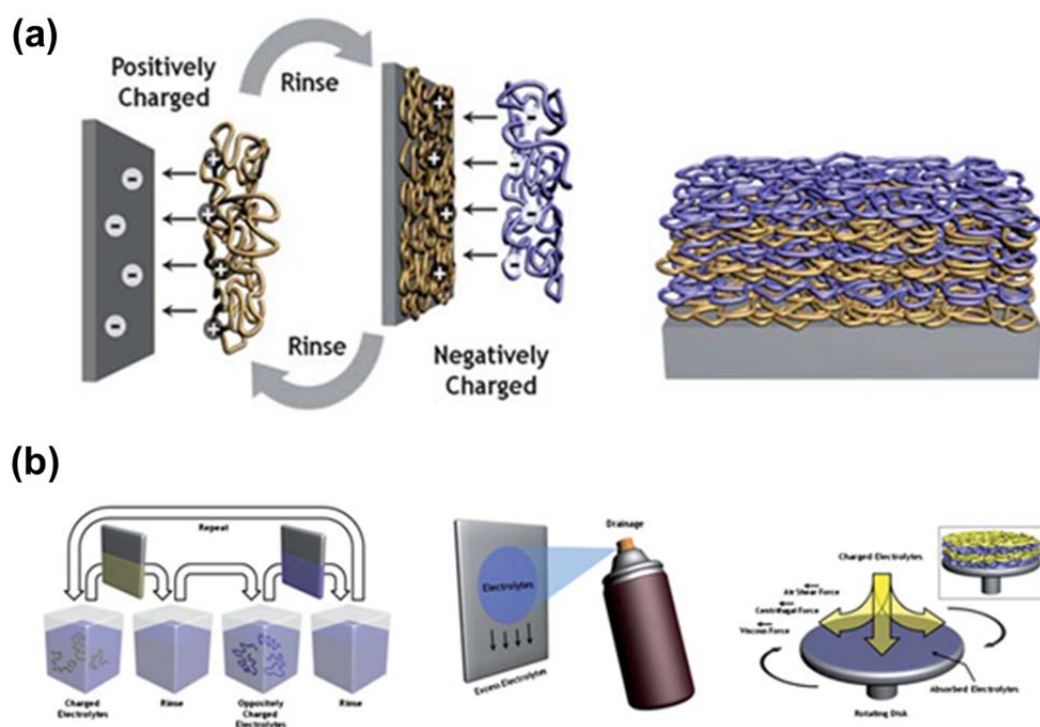


Figure 4 (a) Schematic illustration of the layer-by-layer (LbL) assembled multilayer film deposition process based on electrostatic interaction and a simplified multilayer film built up from a negatively charged substrate. (b) A schematic illustration of the multilayer film deposition process based on the dipping, spraying, and consecutive spinning process of anionic and cationic polyelectrolytes.⁷¹

II. EXPERIMENT

2.1 Preparation of polyaniline (PANi) suspension

The polyaniline suspension was prepared by the method reported previously.⁷² The emeraldine base form of polyaniline (M_w 20000, Aldrich) was dissolved in dimethylacetamide (DMAc) at a concentration of 20 mg/mL by stirring the solution overnight and then bath sonicating for 10 h. The fine particulates were removed by filtering the solution through plain filter paper. The polyaniline dipping solution was prepared by slowly adding one part (by volume) of the filtered polyaniline solution to nine parts of pH-adjusted water (pH 3.0). The pH was then quickly lowered to 2.5 by adding a few drops of 1.0 M HCl solution. The solution was filtered through a 0.45 mm filter again prior to use. The polyaniline dipping solutions were typically used within 2 days of preparation, as they otherwise form irreversible aggregates.

2.2 Preparation of graphene oxide (GO) suspension

Graphite oxide was synthesized from graphite powder (Aldrich, <20 mm) by the modified Hummers method and exfoliated to give a brown dispersion of graphene oxide (GO) under ultrasonication. The GO powder dissolved in a known volume of water is subjected to ultrasonication for 40 min to give a stable suspension of GO (typically conc. 0.50 mg/mL) and then centrifuged at 4000 rpm for 10 min to remove any aggregates remaining in the suspension.

2.3 Fabrication of layer-by-layer assembled (PANi/GO)_n multilayer films

We prepared the two solutions of opposite charges of PANi and GO with pH 2.5 and 3.5 adjusted by 0.1 M HCl, respectively. The as-cleaned substrates were first dipped into a PANi solution for 15 min and then washed in three baths of deionized water (pH 2.5) for 1 min each, to remove residuals and weakly adsorbed PANi. Then, the substrates were dipped into a GO solution for 15 min and washed in the same way with deionized water adjusted to pH 3.5. This cycle makes one bilayer of PANi/GO film, and controls the thickness and formation by repeating the cycles from nanometer to micrometer scale. To enhance the mechanical stability and electrical conductivity of the assembled PANi/GO films, we annealed the as-prepared samples at 150 °C for 12 h in a vacuum oven. To further improve the graphene properties, we conducted a vapor chemical reduction by using hydrazine monohydrate ($N_2H_4 \cdot H_2O$) at 70 °C for 24 h with N_2 flow.

2.4 Fabrication of electropolymerized PANi electrode

Aniline monomer was in situ electropolymerized on an ITO-coated glass substrate in aqueous 1.0 M H_2SO_4 electrolyte containing 0.5 M aniline by a cyclic potential sweep between -0.6 and 1.4 V versus a saturated calomel electrode (SCE) at a scan rate of 100 mV/s.⁷³ After electropolymerization, the PANi electrode was extensively washed with deionized water and dried. The degree of

polymerization of PANi could be controlled by the number of potential sweep cycles. After 20 cycles, the electropolymerized PANi film has 69.23 mg/cm² active mass, which was calculated with a quartz crystal microbalance. The galvanostatic charge–discharge curves were conducted in 1.0 M H₂SO₄ aqueous electrolyte in the range from -0.2 to 0.8 V vs an Ag/AgCl reference electrode with 3 A/g of constant discharge current density for 500 cycles.

2.5 Preparation of electrodes and electrochemical measurements

(PANi/GO)_n films were assembled on an ITO-coated glass substrate and were directly used as a working electrode in a three electrode test cell. Platinum wire and Ag/AgCl were used as a counter and reference electrode, respectively. The characterization of the electrochemical performance for the as-prepared PG_n electrode was conducted using a VMP3 electrochemical potentiostat (BioLogic Inc.). Cyclic voltammograms (CVs) and the galvanostatic charge–discharge process were measured with a potential window from -0.2 to 0.8 V versus Ag/AgCl in 1.0 M H₂SO₄ aqueous electrolyte with wide scan rates from 10 to 200 mV/s and a discharge current density from 0.5 to 3 A/g. We also conducted quartz crystal microbalance (QCM) measurements to acquire the active mass on the electrode, depending on the number of bilayers and post-treatments. The active mass can be calculated using the following Sauerbrey equation:

$$\Delta \text{ mass} = \frac{-\Delta \text{ freq} \times A \times \sqrt{\mu_q \times \rho_q}}{2 \times F_q \times F_q}$$

$$\Delta \text{ mass} = -\Delta \text{ freq} \times 5.453 \times A$$

where Δmass is the mass change (g), Δfreq is the resonant frequency change (Hz), μ_q is AT-cut quartz crystal constant (2.947×10^{11} g/cm³·s²), ρ_q is the quartz crystal density (2.648 g·cm³), F_q is the reference frequency (9.00 MHz), and A is the surface area of the electrode (cm²). The active mass of the electrodes of annealed (GO/GO)₁₀, as-prepared (PANi/GO)₁₀, and heat-treated (PANi/GO)₁₀ are 1.35, 43.63, and 38.81 mg within a specific area (1.4 cm²), respectively. Consequently, the specific capacitance can be calculated by dividing the gravimetric capacitance by a specific surface area.

2.6 Other characterization methods

The growth and structure of the (PANi/GO)_n films were analyzed using UV/vis absorption spectra (Varian, Cary 5000) and X-ray photoelectron spectroscopy (XPS, Thermo Fisher, K-alpha). The thickness of the as-prepared samples on the silicon substrates was measured by ellipsometry (J. A. Woollam Co. Inc., EC-400 and M-2000V). The surface morphology of the prepared electrodes was examined using an atomic force microscope (AFM, Dimension D3100, Veeco) *via* tapping mode and the surface morphology and interior structure of the hybrid films of (PANi/GO)_n were investigated

using a field emission scanning electron microscope (FESEM, FEI, Nanonova 230) and a transmission electron microscope (TEM, JEOL JEM-2100, accelerating voltage of 200 kV, Gatan CCD camera).

III. RESULTS AND DISCUSSION

A supercapacitor can be classified according to the charge storage mechanism as well as the active materials. The first is electric double-layer capacitors (EDLCs) use carbon-based active materials with high surface area, which can store the charge by electrostatically reversible adsorption of electrolyte ions onto active materials. It exhibits an electrochemically stable and high accessible surface area; however, its relatively low capacity is not enough to alternating the secondary batteries. The second is pseudo- or redox capacitors by using the transition metal oxide and electrically conducting polymer as active materials, which exhibit a much high specific capacitance by fast and reversible redox reactions at the surface of active materials. However, it often suffers from a lack of stability during charge/discharge process. The hybrid supercapacitor, which combined each system of electric-double layer capacitor and pseudocapacitor, is a promising approach through the synergistic effects to enhancing their electrochemical performance. We prepared the hybrid electrode, consisting of pseudocapacitive conducting polymer, PANi, and electric-double layer capacitor of graphene nanosheets by Layer-by-Layer (LbL) assembly (**Scheme 1**).

3.1 Layer-by-Layer assembly for hybrid PANi/GO electrodes

To introduce the graphene nanosheet into an LbL system based on intermolecular electrostatic interactions, a graphene oxide (GO) suspension was prepared from a commercial graphite powder followed by the modified Hummer's method.^{51, 74} Following physical exfoliation of the graphite oxide to making a homogeneous dispersion in aqueous solution, the chemical functional groups introduced on the surface of the graphene sheet, such as carboxylic acids, hydroxyl, and epoxide groups, render the prepared GO suspension negatively charged over a wide range of pH conditions. Separately, a positively charged stable polyaniline (PANi) suspension was prepared by dissolving an emeraldine base form of PANi (M_w 20000) in dimethylacetamide (DMAC) with subsequent dilution with pH 2.5 adjusted water (DMAC : H₂O = 1 : 9 v/v) based on the literature protocol.⁷² It should be noted that the pH window for the PANi is limited to 2.5–3.0, whereas that of GO is wide in the range of 1–12 in order for each suspension to remain stable during the assembly. With these two stable suspensions, we fabricated the hybrid thin films by alternately dip-coating on ITO-coated glass substrates or silicon wafers to afford the multilayered architecture of (PANi/GO)_n (n = number of bilayers, typically 2–10, hereafter PG_n) (**Figure 5**).

The successful growth of PG_n multilayers was monitored from a gradual increase of the UV/vis absorbance spectra with the characteristic absorbance of each component (**Figure 5a**). In addition to the absorption at 220 nm due to the presence of GO, there are two absorption bands at 319 and 458 nm corresponding to PANi. The peak at 319 nm can be attributed to the π - π^* transition of benzenoid rings and the broad band at 458 nm is due to the polaron transition, which is a typical characteristic of the conducting emeraldine state of PANi.^{75, 76} Consistent with the UV/vis absorption spectra, the

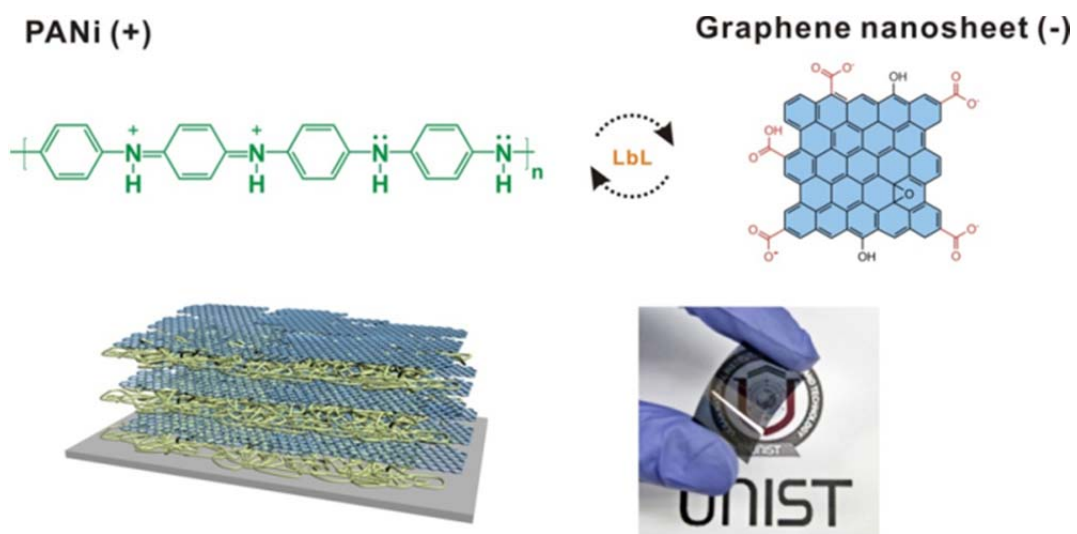
ellipsometry thickness measurements show that the thickness of the PG_n multilayers is linearly proportional to the number of bilayers, demonstrating the uniform and well-controlled assembly of the PG_n thin films with nanoscale precision (**Figure 5b**). From the linear fitting of the curves, an average bilayer thickness of ca. 19 nm was calculated, which is far beyond the thickness of a single layer GO nanosheet (ca. 0.7 nm), suggesting a non-typical superlinear growth of the multilayer films due to the interdiffusion of partially charged PANi within the multilayer films.⁷⁷⁻⁸⁰ We have further observed the tunable growth of PG_n multilayers with respect to the changes in the pH of the GO suspension at a fixed pH of PANi (pH 2.5). For instance, upon increasing the pH of the GO suspensions from 3.5 to 6.5, we found that the growth of the PG_n multilayer film decreased, as monitored by the UV/vis spectra (**Figure 5c**). This is due to the surface charge increase of carboxylic acid groups in the GO suspension, leading to less adsorption on the pre-adsorbed positively charged PANi layer to balance the surface charges. This type of pH tailorable behavior of LbL thin films was similarly observed with weak polyelectrolytes, as well as with other nanomaterials, where pH can alter the degree of ionization and eventually lead to differences in the film thickness and morphology of the resulting LbL films.^{81, 82}

3.2 Post-reduction treatments on hybrid PANi/GO electrodes

In order to enhance the mechanical integrity of the multilayer films to the substrate and to improve the electrical properties of the graphene nanosheets, the as-assembled hybrid multilayers of PG_n were subjected to thermal reduction at 150 °C for 12 h under vacuum to yield heat-treated PG_n samples (hereafter PG_n -H). Additional chemical reduction of the PG_n -H films *via* gaseous hydrazine monohydrate at 70 °C for 24 h afforded samples of both heat- and chemical-treated PG_n (hereafter PG_n -HC) with considerably enhanced electrical conductivity of the graphene nanosheets. After thermal reduction, the PG_n -H films appeared dark blue, resulting from partial restoration of the conjugated aromatic structure within the graphitic structure, whereas the color of the PG_n -HC films changed to dark green, reflecting the changes in the electronic state of PANi that may occur during the chemical reduction process (**Figure 5d**). The UV/vis spectra of GO in the as-assembled PG_n film was also red-shifted to 275 and 268 nm after thermal and chemical reduction, respectively, which demonstrates the successful restoration of electronic conjugation within the graphene sheets.⁷⁴

3.3 Characterization of the structural and chemical properties of hybrid PANi/GO electrodes

The side-on scanning electron microscopy (SEM) image shows the surface is covered with a uniform film of PG_n multilayers (**Figure 6a**). The surface morphology of the as-assembled film exhibits stacked multilayered structure of the graphene nanosheets (**Figure 6b**). The elemental mapping image further supported the uniform distribution of carbon, oxygen, and nitrogen over the entire multilayer characteristic wrinkled graphene sheets that are distributed over the entire film



Scheme 1. Schematic representation of layer-by-layer (LbL) assembled multilayer thin film of PANi with graphene oxide nanosheets with a photograph of the film assembled on a flexible PET substrate.

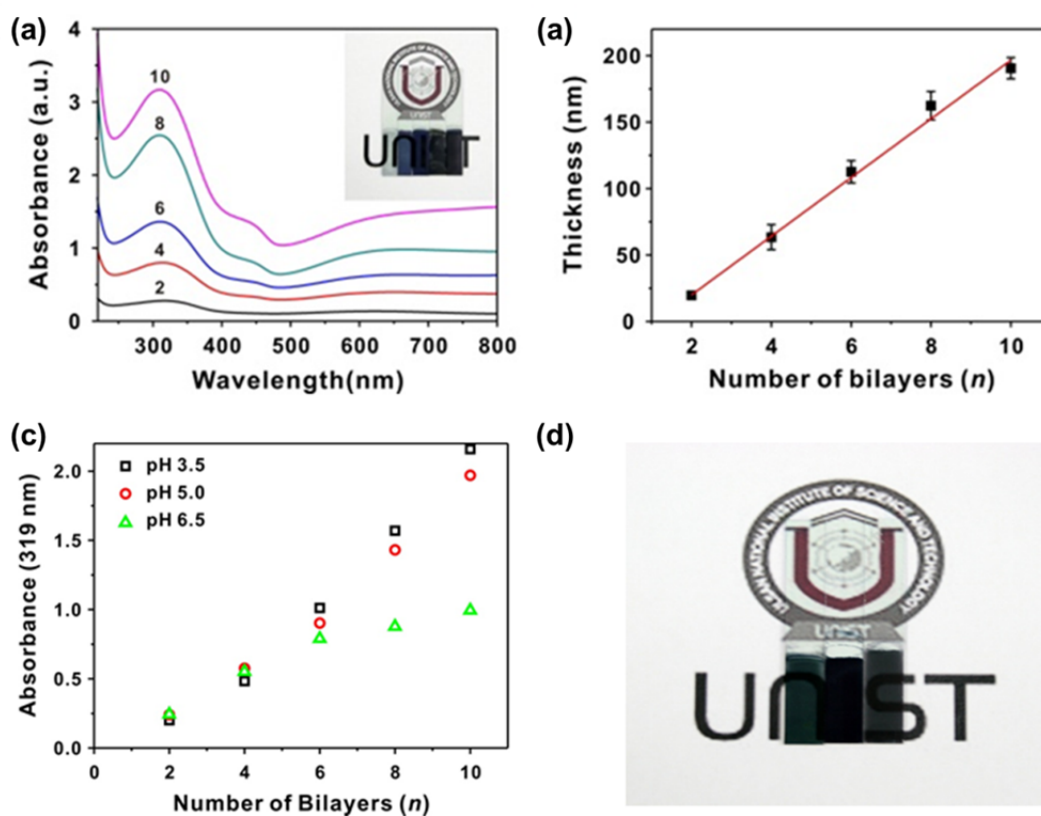


Figure 5. (a) UV/vis spectra and (b) ellipsometry thickness of as-assembled (PANI/GO)_n multilayer films as a function of the number of bilayers. The number on each graph represents the number of bilayer (*n*). Inset in Fig 5a is the image of corresponding samples from 2- to 10-bilayer. Thickness is the average values of five independent measurements. (c) Plot of the UV/vis absorption peak at 319 nm of PG_n multilayer film as a function of the number of bilayers constructed with varying pH of GO suspension at a fixed pH of PANi (pH 2.5). (d) Representative photograph image of LbL-assembled hybrid electrodes of (left) PG₁₀ (middle) PG₁₀-H, and (right) PG₁₀-HC.

surface. The internal microstructure was investigated with transmission electron microscopy (TEM), which revealed the films, confirming the presence of both PANi (a source of carbon and nitrogen) and GO (a source of carbon and oxygen) within the multilayer films (**Figure 6c**). The atomic force microscopy (AFM) image of the as-assembled PG_n film displays a similar microstructure of the graphene sheets covered with a polymeric PANi structure without significant phase separation. Moreover, the surface morphology of the as-assembled PG₁₀ film was further compared with those of PG₁₀-H and PG₁₀-HC (**Figure 6d-f**). Although we could not determine distinctive differences in the surface morphology relating to the post-treatments, we found that the film thickness diminished significantly from 192 ± 3.2 nm (PG₁₀) to 135 ± 0.82 nm (PG₁₀-H) and 132 ± 0.65 nm (PG₁₀-HC) from ellipsometry. Similarly, the root-mean-squared surface roughness (R_{rms}) decreased slightly from 16.7 nm (PG₁₀) to 15.6 nm (PG₁₀-H) and 15.7 nm (PG₁₀-HC) after respective post-treatment processes. Taken together, the post-thermal and chemical treatments induced close packing between the PANi and GO layers *via* evaporation of intercalated water and removal of the oxygen containing functional groups in the as-assembled PG₁₀ film.

X-ray photoelectron spectroscopy (XPS) studies were employed to monitor the progress of the characteristic binding energy of the C1s and N1s peaks corresponding to each functional group present on the graphene nanosheets and PANi (**Figure 7 and Table 1**). On the basis of the XPS data, the atomic composition of the surface of the films was determined to be 72.93% carbon, 21.18% oxygen, and 5.89% nitrogen in the as assembled PG₁₀ film. This survey scan allows the calculation of the relative fraction of PANi which is approximately 41.2% within the multilayer PG₁₀ film. Deconvolution of the high-resolution spectra of C1s further affords six distinct components corresponding to the graphitic carbon framework for sp² (C=C) (284.4 eV) and sp³ (C-C) (285.1 eV), C-N in the backbone of PANi (285.8 eV), C-O in epoxy and hydroxyl (286.6 eV), carbonyls (288.0 eV), and carboxylic acids (289.9 eV), which can be attributed to GO, as reported previously (**Figure 7a**).^{64,83} After thermal and chemical reduction treatments, the fraction of sp²-carbon increased from 48.3 to 57.4 and 59.8%, respectively, supporting the effective recovery of the graphitic structures, as observed also in the UV/vis spectra. Moreover, it is interesting to note that the composition of the C-N peak increased sharply upon chemical reduction, which is partly due to the substitution of nitrogen from the hydrazine monohydrate on the edge plane of the graphene sheets.⁸⁴ In agreement with the above results, high-resolution N1s spectra further yielded detailed structural information of PANi within the multilayer. For example, **Figure 7b** shows that most of the nitrogen atoms in PANi are in the form of benzenoid amine (-NH-) centered at 399.37 eV with additional small peaks, including those of quinoid imine (=N-) (398.21 eV), and positively charged nitrogen atoms (N⁺) (401.09 eV).⁸⁵⁻
⁸⁷ Although we could not observe new peaks arising after the thermal and chemical treatments, the fraction of the quinoid imine to the benzenoid amine peak (=N-/-NH-) increased modestly from 0.22 (PG₁₀) to 0.25 (PG₁₀-H) upon thermal treatment. On the contrary, this ratio drops drastically to 0.08

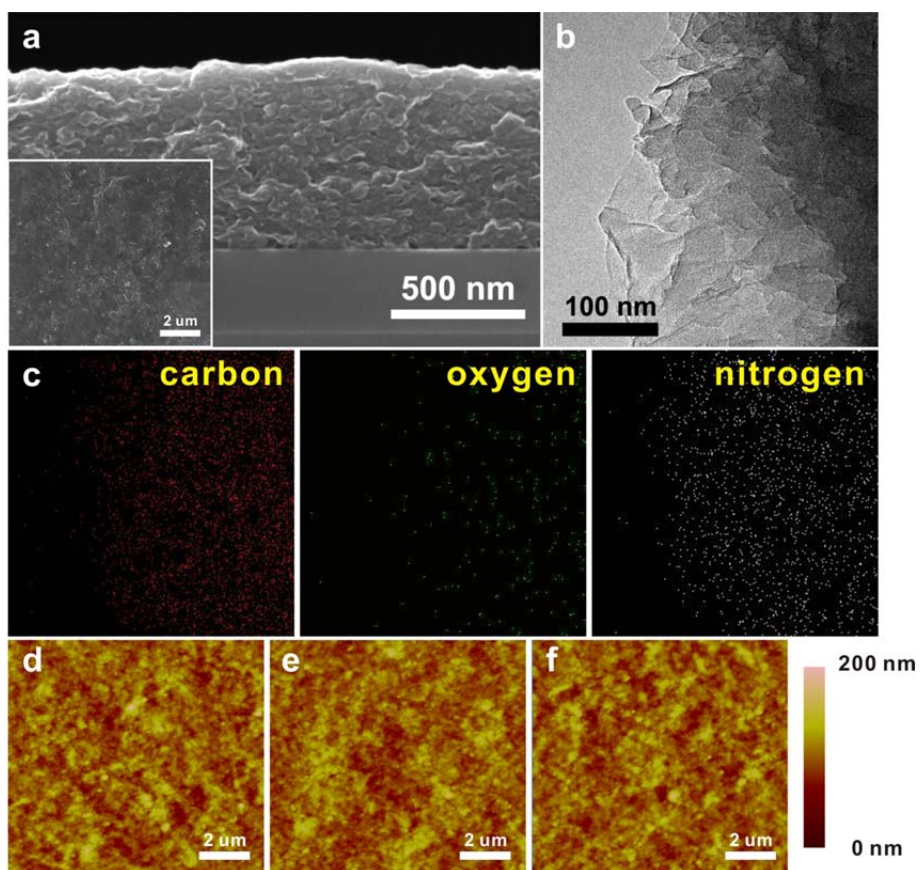


Figure 6. Representative images of as-assembled PG_{20} multilayer films: (a) SEM and (b,c) TEM with a corresponding elemental mapping. Inset in (a) shows the surface morphology. (d-f) Height-mode AFM images of (d) as-assembled PG_{10} , (e) heat treated PG_{10} -H, and (f) both heat- and chemical-treated PG_{10} -HC.

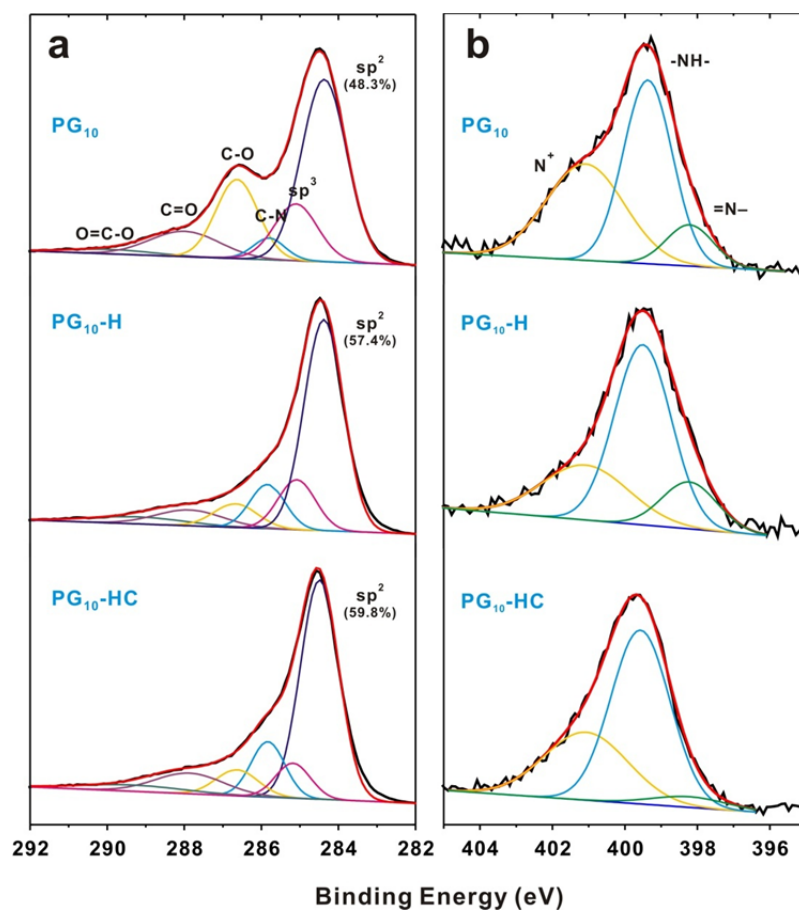


Figure 7. High-resolution (a) C1s and (b) N1s XPS spectra of all (PANI/GO)₁₀ multilayer films with and without post-treatments. The percentage under the sp² label in Fig 7a represents the fraction of sp²-carbon.

Table 1. XPS peak assignments of deconvoluted C 1s and N 1s composition with relative percentage of each peak.

| | Binding Energy (eV) / relative percentage (%) | | | | | | | | |
|---------------------------|---|---------|---------|---------|---------|--------|---------|---------|----------------|
| | C 1s | | | | | | N 1s | | |
| | C=C | C-C | C-N | C-O | C=O | O-C=O | =N- | -NH- | N ⁺ |
| PG₁₀ | 284.37 | 285.1 | 285.8 | 286.63 | 287.95 | 289.89 | 398.21 | 399.37 | 401.09 |
| | (48.32) | (14.96) | (4.37) | (19.71) | (10.43) | (2.21) | (10.53) | (48.85) | (40.62) |
| PG₁₀-H | 284.38 | 285.08 | 285.84 | 286.67 | 287.87 | 289.23 | 398.22 | 399.5 | 401.09 |
| | (57.37) | (12.89) | (10.7) | (7.1) | (7.31) | (4.63) | (9.68) | (58.2) | (27.11) |
| PG₁₀-HC | 284.45 | 285.16 | 285.83 | 286.63 | 287.87 | 289.36 | 398.21 | 399.57 | 401.07 |
| | (59.79) | (8.27) | (12.76) | (7.05) | (7.64) | (4.48) | (4.81) | (61.26) | (33.93) |

after further chemical reduction in PG₁₀-HC, suggesting a lower overall doping level of the PANi chain in the PG₁₀-HC film compared to that in the PG₁₀ and PG₁₀-H films, albeit the GO is reduced accordingly. In conjunction with this observation, Maser et al. recently reported that the simultaneous reduction of a GO and PANi composite by hydrazine produced a solid-state charge-transfer complex possessing a lower number of quinoid groups compared to benzenoid groups. Additionally, the relative fraction of radical cationic nitrogen at 401.09 eV decreased from 40.62 (PG₁₀) to 27.11 (PG₁₀-H) and 33.93% (PG₁₀-HC), reflecting the influence of the post-thermal and chemical treatment on the doping level of the PANi structure.

3.4 Electrochemical performance of hybrid PANi/GO electrodes for supercapacitor

To evaluate the electrochemical properties and quantify the specific capacitance of the various samples prepared in this study, we performed cyclic voltammetry (CV) measurements in 1.0 M H₂SO₄ electrolyte using a three-electrode configuration with platinum wire and Ag/AgCl as a counter and a reference electrode, respectively.

In order to exclude the contribution of pseudocapacitive PANi within the hybrid electrode, we also assembled a (GO/GO)₁₀ multilayer electrode as a control which was composed exclusively of graphene nanosheets according to the method described in our previous reports.⁸⁸⁻⁹¹ This all graphene multilayer of the (GO/GO)₁₀ sample was heat-treated at 150 °C for 12 h to enhance adhesion of the film to the substrate during the electrochemical cycles and to increase the conductivity of the multilayer films.

As shown in **Figure 8**, all samples of the (PANi/GO)₁₀ hybrid films assembled on ITO-coated glass substrates exhibited broad redox peaks in the potential range of -0.2 to 0.8 V investigated. In particular, all hybrid electrodes displayed the typical pseudocapacitive behavior of PANi incorporated within the hybrid electrodes. Peaks for C₁/A₁ are attributed to the redox transition of PANi between a semiconductive state (leucoemeraldine) and a conducting state (polaronic emeraldine), and the additional redox peaks for C₂/A₂ are associated with the faradaic transformation of emeraldine to pernigraniline.^{57, 63, 92} It is also observed that there is a positive shift of the cathodic peaks (C₁/C₂) and a negative shift of the anodic peaks (A₁/A₂) with increasing potential scan rate (**Figure 8**). The specific capacitance (C_{sp}) of the electrode can be calculated according to the following equation:

$$C_{sp} = \frac{1}{mv(V_f - V_i)} \int_{V_i}^{V_f} I(V)dV$$

where I is the response current (A), V_f and V_i are the integration potential limits (V) of the voltammetric curve, v is the potential scan rate (V/s), and m is the mass of the active electrode material measured by a quartz crystal microbalance (QCM) (g). Based on the above equation, we

found a C_{sp} of 402.5–219.4 F/g (PG₁₀), 489.0–304.8 F/g (PG₁₀-H), 240.1–103.5 F/g (PG₁₀-HC), and 24.6–10.9 F/g (GG₁₀-H), respectively, at scan rates in the range of 10 to 200 mV/s (**Table 2**).

We also observed that the intermediate capacitive behavior of PG₁₀ increased upon thermal of PANi with two characteristic sets of redox peaks (C_1/A_1 and C_2/A_2) related to the redox transition treatments to PG₁₀-H owing to the recovery of the electrical conductivity of the graphene nanosheets, which affected the electrochemical properties of the supercapacitors. On the other hand, further chemical treatment did not improve its electrochemical performance, although the chemical reduction can effectively recover the electrical properties of the graphene nanosheets. We postulate that the chemical treatment with hydrazine can also influence the conducting level of PANi, as monitored from the relatively low ratio of quinoid imine to benzenoid amine from the XPS spectra in **Figure 7**, which diminishes the electrochemical performance of the hybrid electrode. In addition, it is hard to exclude the possibility of structural degradation of PANi during the chemical reduction process.

In clear contrast to the hybrid electrode, the assembled all-GO electrode without PANi exhibited a nearly ideal rectangular shape without any obvious redox peaks, which corresponds to a characteristic electric double-layer capacitive (EDLC) behavior with a specific capacitance of 10.9 F/g at a scan rate of 200 mV/s. According to the report of Hammond and Shao-Horn, multilayer thin films of all multiwalled carbon nanotubes (MWNTs) exhibit a similar rectangular capacitive behavior with a small portion of pseudocapacitive redox peaks associated with the surface functional groups attached to the surface of MWNTs such as carboxylic acid groups.⁹³ Taken together, our hybrid system of PANi with graphene nanosheets contributed to the significant enhancement of the electrochemical performance through a synergistic effect, in which the high specific surface area and electrical conductivity of the graphene nanosheets that are coupled with the redox transition from PANi for decreased diffusion length and fast electron transfer at the interface between the electrodes and the electrolyte ions.

As shown in **Figure 9**, the galvanostatic charge–discharge curves and specific capacitance with cyclic stability of the PG₁₀ and PG₁₀-H hybrid electrodes conducted as a function of discharge current density from 0.5 to 3.0 A/g. The specific capacitance based on the galvanostat is calculated by the following equation:

$$C_{sp}(\text{F/g}) = (i \times \Delta t) / (\Delta E \times m)$$

where i is the discharge current (A), Δt is discharge time (s), ΔE is the voltage difference (V), and m is the active mass of electrode. According to equation, we found that the thermally annealed PG₁₀-H electrode has a much higher capacity of 116.5–375.2 F/g than does the as-assembled PG₁₀ electrode of 94.2–162.9 F/g over the entire range of discharge current density (0.5–3.0 A/g) in accord with the C_{sp} measured from the CV (**Table 2**). Moreover, based on the above values, we calculated that the energy

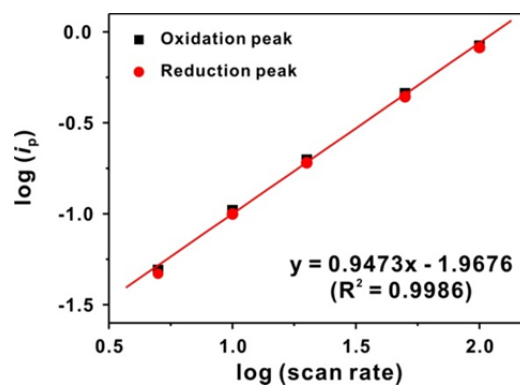
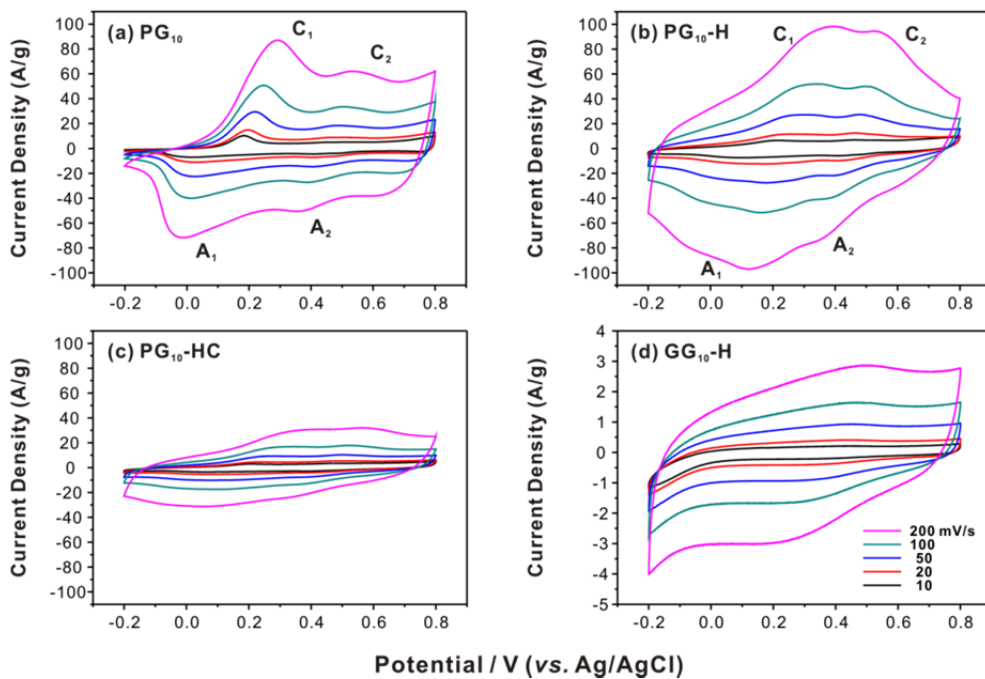


Figure 8. (Top) Cyclic voltammogram (CV) curves of all $(\text{PANi}/\text{GO})_n$ hybrid electrode films with various scan rates from 10 to 200 mV/s. (a) As-prepared PG_{10} , (b) heat-treated $\text{PG}_{10}\text{-H}$, (c) heat- and chemically-treated $\text{PG}_{10}\text{-HC}$, and (d) heat-treated $(\text{GO}/\text{GO})_{10}$. All electrochemical properties were collected in a three-electrode system with a Ag/AgCl reference in 1.0 M H_2SO_4 electrolyte at identical scan rates presented in (d). Note that the y-scale in (d) is significantly smaller than the others. (Bottom) Plot of the peak current density (mA/cm^2) vs potential scan rate (mV/s) of $\text{PG}_{10}\text{-H}$ in an equi-span log-log scale. The slopes were estimated to be around 1.0 for both cases.

Table 2 Specific capacitance values of hybrid PG₁₀, PG₁₀-H, PG₁₀-HC, and GG₁₀-H electrodes obtained from cyclic voltammograms and galvanostat charge/discharge experiments.

| | Specific capacitance (F/g) (from cyclic voltammograms) | | | | |
|---------------------------|---|---------|---------|----------|----------|
| | 10 mV/s | 20 mV/s | 50 mV/s | 100 mV/s | 200 mV/s |
| PG₁₀ | 402.48 | 326.17 | 269.18 | 241.54 | 219.35 |
| PG₁₀-H | 489.04 | 400.13 | 349.92 | 323.76 | 304.76 |
| PG₁₀-HC | 240.13 | 180.53 | 135.01 | 116.85 | 103.54 |
| GG₁₀-H | 24.62 | 19.08 | 15.3 | 12.84 | 10.94 |

| | Specific capacitance (F/g) (from charge/discharge curves) | | | | | |
|--------------------------|--|--------|---------|---------|---------|---------|
| | 0.5 A/g | 1 A/g | 1.5 A/g | 2.0 A/g | 2.5 A/g | 3.0 A/g |
| PG₁₀ | 162.89 | 136.24 | 121.04 | 103.64 | 101.15 | 94.23 |
| PG₁₀-H | 375.15 | 218.43 | 163.92 | 129.92 | 124.65 | 116.46 |

density of each PG₁₀ and PG₁₀-H electrodes reach 18.92 and 30.34 Wh/kg, respectively, at a power density of 1.0 kW/kg (see **Ragone plot in Figure 10**). It is of note that the thermally annealed PG₁₀-H electrode showed a lower IR drop during the discharge compared to that of the PG₁₀ electrode, clearly indicating the close packed structure and improved electrical conductivity of the active materials *via* thermal reduction effectively decreased the internal resistance in the assembled hybrid electrode. It has also been suggested that a well-ordered nanostructure can reduce the ionic diffusion path, facilitate ionic motion to the inside of the film, and improve the utilization of the electrode materials.⁹⁴

⁹⁵ Due to the instability and lack of adhesion to the substrate of PG₁₀-HC during repeated charge–discharge cycles, we could not obtain reproducible data for PG₁₀-HC, unfortunately. Furthermore, we examined the cycling stability of the prepared hybrid electrodes using a galvanostatic charge–discharge test. Interestingly, the PG₁₀-H electrode demonstrates a considerably better cycling stability up to 500 cycles with 90.7% retention of the initial capacitance compared to that of the as-assembled PG₁₀ electrode (78.4% retention) at a discharge current density of 3 A/g. It should be noted that although the capacitance retention of the pure GO multilayer film is still better after 500 cycles (99.8%), the preservation of the capacitive behavior of the hybrid electrode is radically improved when compared with that of pure electropolymerized PANi (only 28.3% after mere 10 cycles) (**Figure 9d**). These results suggest that the presence of a partially reduced graphene nanosheet within the hybrid electrode not only improved the electrical conductivity, but also served as a functional dopant to PANi with an enhanced chemical stability during the charge–discharge process, thereby contributing to the excellent electrochemical performance for supercapacitors.

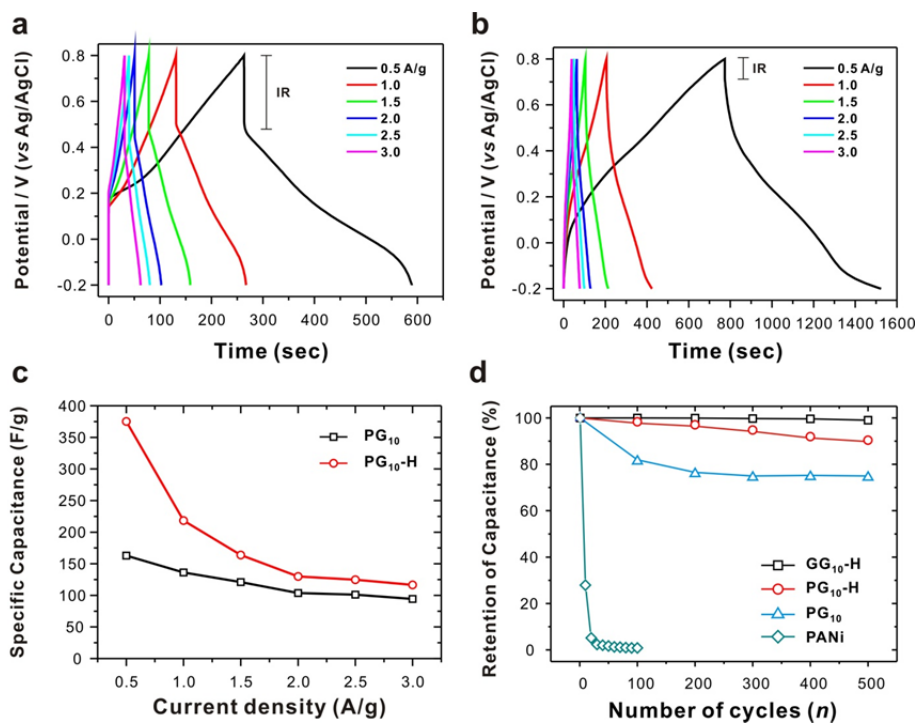


Figure 9. Galvanostat charge/discharge curves of the assembled hybrid (PANI/GO)₁₀ electrodes. (a) PG₁₀, (b) PG₁₀-H, and (c) specific capacitance values as a function of discharge current density from 0.5 to 3 A/g. (d) Comparison of cycling stability of all samples at a high discharge current density of 3 A/g. Electropolymerized pure PANi film was used for comparison.

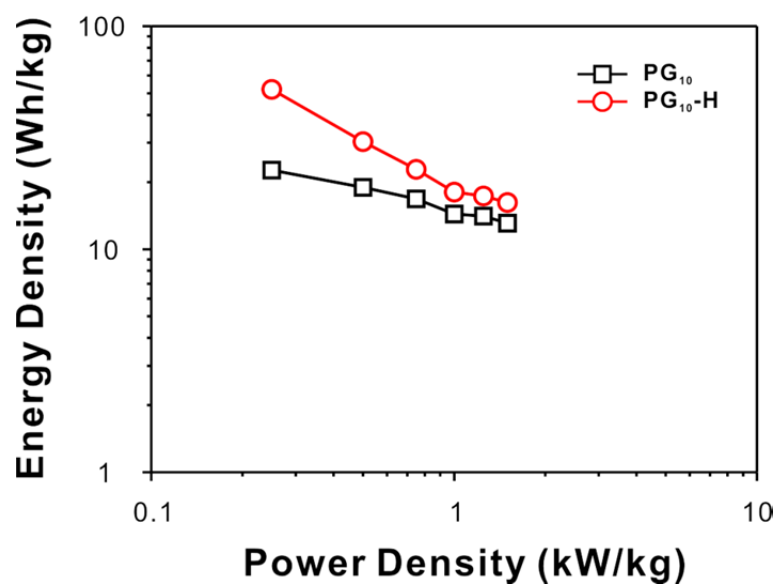


Figure 10. Ragone plot of the LbL-assembled hybrid PG₁₀ (black-line) and PG₁₀-H (red-line) supercapacitor electrodes measured at different discharge current density from 0.5 to 3 A/g.

IV. CONCLUSION

In conclusion, we have developed a simple method of fabricating hybrid thin film supercapacitors of polyaniline (PANi) and graphene oxide (GO) nanosheets by nanoscale blending layer-by-layer (LbL) assembly based on electrostatic interactions. The hybrid electrode prepared by the LbL method not only offers precise control over the thickness, internal structure and flexibility, but also enhanced chemical stability and electronic conductivity during the charge–discharge process, benefiting from each component synergistically. We found that the LbL assembled PANi with GO nanosheets thin film after thermal treatment could exhibit an excellent gravimetric capacitance of 375.2 F/g at a 0.5 A/g discharge current density that outperformed many other hybrid supercapacitors reported to date and maintained its capacity up to 90.7% over 500 cycles at a high current density of 3.0 A/g. The current work highlights how LbL assembly can be applied to produce nanoscale intimate interfaces at the electroactive blends of graphene nanosheets with polymeric materials. We anticipate that this platform technique will offer the potential to address critical questions on the fundamental relationship between structure and energy storage properties, as well as bridging the performance gap that currently exists between batteries and capacitors for the future.

REFERENCES

1. Winter, M.; Brodd, R. J., What Are Batteries, Fuel Cells, and Supercapacitors? *Chem. Rev.* **2004**, *104*, 4245-4270.
2. Arico, A. S.; Bruce, P.; Scrosati, B.; Tarascon, J.-M.; van Schalkwijk, W., Nanostructured materials for advanced energy conversion and storage devices. *Nat. Mater.* **2005**, *4*, 366-377.
3. Guo, Y.-G.; Hu, J.-S.; Wan, L.-J., Nanostructured Materials for Electrochemical Energy Conversion and Storage Devices. *Adv. Mater.* **2008**, *20*, 2878-2887.
4. Conway, B. E., Transition from “Supercapacitor” to “Battery” Behavior in Electrochemical Energy Storage. *J. Electrochem. Soc.* **1991**, *138*, 1539-1548.
5. Conway, B., *Electrochemical supercapacitors: scientific fundamentals and technological applications*. Kluwer Academic/plenum. New York: 1999.
6. Kötz, R.; Carlen, M., Principles and applications of electrochemical capacitors. *Electrochim. Acta* **2000**, *45*, 2483-2498.
7. Frackowiak, E.; Béguin, F., Carbon materials for the electrochemical storage of energy in capacitors. *Carbon* **2001**, *39*, 937-950.
8. Simon, P.; Gogotsi, Y., Materials for electrochemical capacitors. *Nat. Mater.* **2008**, *7*, 845-854.
9. Zhang, L. L.; Zhao, X. S., Carbon-based materials as supercapacitor electrodes. *Chem. Soc. Rev.* **2009**, *38*, 2520-2531.
10. Service, R. F., New 'Supercapacitor' Promises to Pack More Electrical Punch. *Science* **2006**, *313*, 902.
11. Brodd, R. J.; Bullock, K. R.; Leising, R. A.; Middaugh, R. L.; Miller, J. R.; Takeuchi, E., Batteries, 1977 to 2002. *J. Electrochem. Soc.* **2004**, *151*, K1-K11.
12. Armand, M.; Johansson, P., Novel weakly coordinating heterocyclic anions for use in lithium batteries. *J. Power Sources* **2008**, *178*, 821-825.
13. Armand, M.; Tarascon, J. M., Building better batteries. *Nature* **2008**, *451*, 652-657.
14. Miller, J. R.; Burke, A. F., Electrochemical capacitors: challenges and opportunities for real-world applications. *Electrochem. Soc. Interface* **2008**, *17*, 53.
15. Burke, A., Ultracapacitors: why, how, and where is the technology. *J. Power Sources* **2000**, *91*, 37-50.
16. Miller, J. R.; Simon, P., Electrochemical Capacitors for Energy Management. *Science* **2008**, *321*, 651-652.
17. Helmholtz, H., Ueber einige Gesetze der Vertheilung elektrischer Ströme in körperlichen Leitern mit Anwendung auf die thierisch-elektrischen Versuche. *Ann. Phys.* **1853**, *165*, 211-233.
18. Gouy, G., Constitution of the electric charge at the surface of an electrolyte. *J. Phys.* **1910**, *9*, 457-467.

19. Chapman, D. L., LI. A contribution to the theory of electrocapillarity. *Philos. Mag.* **1913**, *25*, 475-481.
20. Stern, O., The theory of the electrolytic double-layer. *Z. Elektrochem.* **1924**, *30*, 508-516.
21. Pandolfo, A. G.; Hollenkamp, A. F., Carbon properties and their role in supercapacitors. *J. Power Sources* **2006**, *157*, 11-27.
22. Zheng, J. P.; Cygan, P. J.; Jow, T. R., Hydrous Ruthenium Oxide as an Electrode Material for Electrochemical Capacitors. *J. Electrochem. Soc.* **1995**, *142*, 2699-2703.
23. Wu, N.-L., Nanocrystalline oxide supercapacitors. *Mater. Chem. Phys.* **2002**, *75*, 6-11.
24. Brousse, T.; Toupin, M.; Dugas, R.; Athouël, L.; Crosnier, O.; Bélanger, D., Crystalline MnO₂ as Possible Alternatives to Amorphous Compounds in Electrochemical Supercapacitors. *J. Electrochem. Soc.* **2006**, *153*, A2171-A2180.
25. Hu, C.-C.; Chang, K.-H.; Lin, M.-C.; Wu, Y.-T., Design and Tailoring of the Nanotubular Arrayed Architecture of Hydrous RuO₂ for Next Generation Supercapacitors. *Nano Lett.* **2006**, *6*, 2690-2695.
26. Zhang, H.; Cao, G.; Wang, Z.; Yang, Y.; Shi, Z.; Gu, Z., Growth of Manganese Oxide Nanoflowers on Vertically-Aligned Carbon Nanotube Arrays for High-Rate Electrochemical Capacitive Energy Storage. *Nano Lett.* **2008**, *8*, 2664-2668.
27. Rudge, A.; Davey, J.; Raistrick, I.; Gottesfeld, S.; Ferraris, J. P., Conducting polymers as active materials in electrochemical capacitors. *J. Power Sources* **1994**, *47*, 89-107.
28. Fan, L. Z.; Hu, Y. S.; Maier, J.; Adelhelm, P.; Smarsly, B.; Antonietti, M., High Electroactivity of Polyaniline in Supercapacitors by Using a Hierarchically Porous Carbon Monolith as a Support. *Adv. Funct. Mater.* **2007**, *17*, 3083-3087.
29. Frackowiak, E., Carbon materials for supercapacitor application. *Phys. Chem. Chem. Phys.* **2007**, *9*, 1774-1785.
30. Lee, J.; Kim, J.; Hyeon, T., Recent Progress in the Synthesis of Porous Carbon Materials. *Adv. Mater.* **2006**, *18*, 2073-2094.
31. Novoselov, K. S.; Geim, A. K.; Morozov, S. V.; Jiang, D.; Zhang, Y.; Dubonos, S. V.; Grigorieva, I. V.; Firsov, A. A., Electric Field Effect in Atomically Thin Carbon Films. *Science* **2004**, *306*, 666-669.
32. Stankovich, S.; Dikin, D. A.; Dommett, G. H. B.; Kohlhaas, K. M.; Zimney, E. J.; Stach, E. A.; Piner, R. D.; Nguyen, S. T.; Ruoff, R. S., Graphene-based composite materials. *Nature* **2006**, *442*, 282-286.
33. Geim, A. K.; Novoselov, K. S., The rise of graphene. *Nat. Mater.* **2007**, *6*, 183-191.
34. Wu, J.; Pisula, W.; Müllen, K., Graphenes as Potential Material for Electronics. *Chem. Rev.* **2007**, *107*, 718-747.
35. Lee, C.; Wei, X.; Kysar, J. W.; Hone, J., Measurement of the Elastic Properties and Intrinsic

Strength of Monolayer Graphene. *Science* **2008**, *321*, 385-388.

36. Kim, K. S.; Zhao, Y.; Jang, H.; Lee, S. Y.; Kim, J. M.; Kim, K. S.; Ahn, J.-H.; Kim, P.; Choi, J.-Y.; Hong, B. H., Large-scale pattern growth of graphene films for stretchable transparent electrodes. *Nature* **2009**, *457*, 706-710.

37. Stoller, M. D.; Park, S.; Zhu, Y.; An, J.; Ruoff, R. S., Graphene-Based Ultracapacitors. *Nano Lett.* **2008**, *8*, 3498-3502.

38. Bolotin, K. I.; Sikes, K. J.; Jiang, Z.; Klima, M.; Fudenberg, G.; Hone, J.; Kim, P.; Stormer, H. L., Ultrahigh electron mobility in suspended graphene. *Solid State Commun.* **2008**, *146*, 351-355.

39. Balandin, A. A.; Ghosh, S.; Bao, W.; Calizo, I.; Teweldebrhan, D.; Miao, F.; Lau, C. N., Superior Thermal Conductivity of Single-Layer Graphene. *Nano Lett.* **2008**, *8*, 902-907.

40. Cai, W.; Zhu, Y.; Li, X.; Piner, R. D.; Ruoff, R. S., Large area few-layer graphene/graphite films as transparent thin conducting electrodes. *Appl. Phys. Lett.* **2009**, *95*, 123115-123113.

41. Li, X.; Zhu, Y.; Cai, W.; Borysiak, M.; Han, B.; Chen, D.; Piner, R. D.; Colombo, L.; Ruoff, R. S., Transfer of Large-Area Graphene Films for High-Performance Transparent Conductive Electrodes. *Nano Lett.* **2009**, *9*, 4359-4363.

42. Dikin, D. A.; Stankovich, S.; Zimney, E. J.; Piner, R. D.; Dommett, G. H. B.; Evmenenko, G.; Nguyen, S. T.; Ruoff, R. S., Preparation and characterization of graphene oxide paper. *Nature* **2007**, *448*, 457-460.

43. Park, S.; Lee, K.-S.; Bozoklu, G.; Cai, W.; Nguyen, S. T.; Ruoff, R. S., Graphene Oxide Papers Modified by Divalent Ions-Enhancing Mechanical Properties *via* Chemical Cross-Linking. *ACS Nano* **2008**, *2*, 572-578.

44. Ramanathan T; Abdala, A. A.; Stankovich S; Dikin, D. A.; Herrera Alonso, M.; Piner, R. D.; Adamson, D. H.; Schniepp, H. C.; Chen X; Ruoff, R. S.; Nguyen, S. T.; Aksay, I. A.; Prud'Homme, R. K.; Brinson, L. C., Functionalized graphene sheets for polymer nanocomposites. *Nat. Nanotechnol.* **2008**, *3*, 327-331.

45. Bunch, J. S.; van der Zande, A. M.; Verbridge, S. S.; Frank, I. W.; Tanenbaum, D. M.; Parpia, J. M.; Craighead, H. G.; McEuen, P. L., Electromechanical Resonators from Graphene Sheets. *Science* **2007**, *315*, 490-493.

46. Xuekun, L.; Minfeng, Y.; Hui, H.; Rodney, S. R., Tailoring graphite with the goal of achieving single sheets. *Nanotechnology* **1999**, *10*, 269.

47. Berger, C.; Song, Z.; Li, X.; Wu, X.; Brown, N.; Naud, C.; Mayou, D.; Li, T.; Hass, J.; Marchenkov, A. N.; Conrad, E. H.; First, P. N.; de Heer, W. A., Electronic Confinement and Coherence in Patterned Epitaxial Graphene. *Science* **2006**, *312*, 1191-1196.

48. Eizenberg, M.; Blakely, J. M., Carbon monolayer phase condensation on Ni(111). *Surf. Sci.* **1979**, *82*, 228-236.

49. Brodie, B. C., On the Atomic Weight of Graphite. *Philos. Trans. R. Soc. London* **1859**, *149*, 249-

259.

50. Staudenmaier, L., Verfahren zur Darstellung der Graphitsäure. *Ber. Dtsch. Chem. Ges.* **1898**, *31*, 1481-1487.
51. Hummers, W. S.; Offeman, R. E., Preparation of Graphitic Oxide. *J. Am. Chem. Soc.* **1958**, *80*, 1339-1339.
52. Park, S.; Ruoff, R. S., Chemical methods for the production of graphenes. *Nat. Nanotechnol.* **2009**, *4*, 217-224.
53. Wang, D.; Choi, D.; Li, J.; Yang, Z.; Nie, Z.; Kou, R.; Hu, D.; Wang, C.; Saraf, L. V.; Zhang, J.; Aksay, I. A.; Liu, J., Self-Assembled TiO₂-Graphene Hybrid Nanostructures for Enhanced Li-Ion Insertion. *ACS Nano* **2009**, *3*, 907-914.
54. Li, S.-S.; Tu, K.-H.; Lin, C.-C.; Chen, C.-W.; Chhowalla, M., Solution-Processable Graphene Oxide as an Efficient Hole Transport Layer in Polymer Solar Cells. *ACS Nano* **2010**, *4*, 3169-3174.
55. Wang, D.; Kou, R.; Choi, D.; Yang, Z.; Nie, Z.; Li, J.; Saraf, L. V.; Hu, D.; Zhang, J.; Graff, G. L.; Liu, J.; Pope, M. A.; Aksay, I. A., Ternary Self-Assembly of Ordered Metal Oxide-Graphene Nanocomposites for Electrochemical Energy Storage. *ACS Nano* **2010**, *4*, 1587-1595.
56. Wang, H.; Cui, L.-F.; Yang, Y.; Sanchez Casalongue, H.; Robinson, J. T.; Liang, Y.; Cui, Y.; Dai, H., Mn₃O₄-Graphene Hybrid as a High-Capacity Anode Material for Lithium Ion Batteries. *J. Am. Chem. Soc.* **2010**, *132*, 13978-13980.
57. Zhang, K.; Zhang, L. L.; Zhao, X. S.; Wu, J., Graphene/Polyaniline Nanofiber Composites as Supercapacitor Electrodes. *Chem. Mater.* **2010**, *22*, 1392-1401.
58. Bai, H.; Li, C.; Shi, G., Functional Composite Materials Based on Chemically Converted Graphene. *Adv. Mater.* **2011**, *23*, 1089-1115.
59. Jang, J., Conducting Polymer Nanomaterials and Their Applications. In *Emissive Materials Nanomaterials*, Springer Berlin Heidelberg: 2006; Vol. 199, pp 189-260.
60. Bai, H.; Xu, Y.; Zhao, L.; Li, C.; Shi, G., Non-covalent functionalization of graphene sheets by sulfonated polyaniline. *Chem. Commun.* **2009**, *0*, 1667-1669.
61. Wu, Q.; Xu, Y.; Yao, Z.; Liu, A.; Shi, G., Supercapacitors Based on Flexible Graphene/Polyaniline Nanofiber Composite Films. *ACS Nano* **2010**, *4*, 1963-1970.
62. Xu, J.; Wang, K.; Zu, S.-Z.; Han, B.-H.; Wei, Z., Hierarchical Nanocomposites of Polyaniline Nanowire Arrays on Graphene Oxide Sheets with Synergistic Effect for Energy Storage. *ACS Nano* **2010**, *4*, 5019-5026.
63. Wang, D.-W.; Li, F.; Zhao, J.; Ren, W.; Chen, Z.-G.; Tan, J.; Wu, Z.-S.; Gentle, I.; Lu, G. Q.; Cheng, H.-M., Fabrication of Graphene/Polyaniline Composite Paper via In Situ Anodic Electropolymerization for High-Performance Flexible Electrode. *ACS Nano* **2009**, *3*, 1745-1752.
64. Feng, X.-M.; Li, R.-M.; Ma, Y.-W.; Chen, R.-F.; Shi, N.-E.; Fan, Q.-L.; Huang, W., One-Step Electrochemical Synthesis of Graphene/Polyaniline Composite Film and Its Applications. *Adv. Funct.*

Mater. **2011**, *21*, 2989-2996.

65. Iler, R. K., Multilayers of colloidal particles. *J. Colloid Interface Sci.* **1966**, *21*, 569-594.
66. Decher, G., Fuzzy Nanoassemblies: Toward Layered Polymeric Multicomposites. *Science* **1997**, *277*, 1232-1237.
67. Caruso, F.; Caruso, R. A.; Möhwald, H., Nanoengineering of Inorganic and Hybrid Hollow Spheres by Colloidal Templating. *Science* **1998**, *282*, 1111-1114.
68. Caruso, F., Nanoengineering of Particle Surfaces. *Adv. Mater.* **2001**, *13*, 11-22.
69. Ostrander, J. W.; Mamedov, A. A.; Kotov, N. A., Two Modes of Linear Layer-by-Layer Growth of Nanoparticle–Polyelectrolyte Multilayers and Different Interactions in the Layer-by-layer Deposition. *J. Am. Chem. Soc.* **2001**, *123*, 1101-1110.
70. Hammond, P. T., Form and Function in Multilayer Assembly: New Applications at the Nanoscale. *Adv. Mater.* **2004**, *16*, 1271-1293.
71. Hong, J.; Han, J. Y.; Yoon, H.; Joo, P.; Lee, T.; Seo, E.; Char, K.; Kim, B.-S., Carbon-based layer-by-layer nanostructures: from films to hollow capsules. *Nanoscale* **2011**, *3*, 4515-4531.
72. Cheung, J. H.; Stockton, W. B.; Rubner, M. F., Molecular-Level Processing of Conjugated Polymers. 3. Layer-by-Layer Manipulation of Polyaniline *via* Electrostatic Interactions. *Macromolecules* **1997**, *30*, 2712-2716.
73. Sazou, D.; Georgolios, C., Formation of conducting polyaniline coatings on iron surfaces by electropolymerization of aniline in aqueous solutions. *J. Electroanal. Chem.* **1997**, *429*, 81-93.
74. Li, D.; Muller, M. B.; Gilje, S.; Kaner, R. B.; Wallace, G. G., Processable aqueous dispersions of graphene nanosheets. *Nat. Nanotechnol.* **2008**, *3*, 101-105.
75. Chen, S.-A.; Hwang, G.-W., Water-Soluble Self-Acid-Doped Conducting Polyaniline: Structure and Properties. *J. Am. Chem. Soc.* **1995**, *117*, 10055-10062.
76. Sheng, K.; Bai, H.; Sun, Y.; Li, C.; Shi, G., Layer-by-layer assembly of graphene/polyaniline multilayer films and their application for electrochromic devices. *Polymer* **2011**, *52*, 5567-5572.
77. Lavalle, P.; Vivet, V.; Jessel, N.; Decher, G.; Voegel, J.-C.; Mesini, P. J.; Schaaf, P., Direct Evidence for Vertical Diffusion and Exchange Processes of Polyanions and Polycations in Polyelectrolyte Multilayer Films. *Macromolecules* **2004**, *37*, 1159-1162.
78. Quinn, J. F.; Yeo, J. C. C.; Caruso, F., Layer-by-Layer Assembly of Nanoblended Thin Films: Poly(allylamine hydrochloride) and a Binary Mixture of a Synthetic and Natural Polyelectrolyte. *Macromolecules* **2004**, *37*, 6537-6543.
79. Yoo, P. J.; Nam, K. T.; Qi, J.; Lee, S.-K.; Park, J.; Belcher, A. M.; Hammond, P. T., Spontaneous assembly of viruses on multilayered polymer surfaces. *Nat. Mater.* **2006**, *5*, 234-240.
80. Zacharia, N. S.; DeLongchamp, D. M.; Modestino, M.; Hammond, P. T., Controlling Diffusion and Exchange in Layer-by-Layer Assemblies. *Macromolecules* **2007**, *40*, 1598-1603.
81. Shiratori, S. S.; Rubner, M. F., pH-Dependent Thickness Behavior of Sequentially Adsorbed

Layers of Weak Polyelectrolytes. *Macromolecules* **2000**, *33*, 4213-4219.

82. Hong, T.-K.; Lee, D. W.; Choi, H. J.; Shin, H. S.; Kim, B.-S., Transparent, Flexible Conducting Hybrid Multilayer Thin Films of Multiwalled Carbon Nanotubes with Graphene Nanosheets. *ACS Nano* **2010**, *4*, 3861-3868.

83. Tang, L.; Wang, Y.; Li, Y.; Feng, H.; Lu, J.; Li, J., Preparation, Structure, and Electrochemical Properties of Reduced Graphene Sheet Films. *Adv. Funct. Mater.* **2009**, *19*, 2782-2789.

84. Park, S.; Hu, Y.; Hwang, J. O.; Lee, E.-S.; Casabianca, L. B.; Cai, W.; Potts, J. R.; Ha, H.-W.; Chen, S.; Oh, J.; Kim, S. O.; Kim, Y.-H.; Ishii, Y.; Ruoff, R. S., Chemical structures of hydrazine-treated graphene oxide and generation of aromatic nitrogen doping. *Nat. Commun.* **2012**, *3*, 638.

85. Fusalba, F.; Bélanger, D., Electropolymerization of Polypyrrole and Polyaniline–Polypyrrole from Organic Acidic Medium. *J. Phys. Chem. B* **1999**, *103*, 9044-9054.

86. Hu, C.-C.; Lin, J.-Y., Effects of the loading and polymerization temperature on the capacitive performance of polyaniline in NaNO₃. *Electrochim. Acta* **2002**, *47*, 4055-4067.

87. Vallés, C.; Jiménez, P.; Muñoz, E.; Benito, A. M.; Maser, W. K., Simultaneous Reduction of Graphene Oxide and Polyaniline: Doping-Assisted Formation of a Solid-State Charge-Transfer Complex. *J. Phys. Chem. C* **2011**, *115*, 10468-10474.

88. Hong, J.; Char, K.; Kim, B.-S., Hollow Capsules of Reduced Graphene Oxide Nanosheets Assembled on a Sacrificial Colloidal Particle. *J. Phys. Chem. Lett.* **2010**, *1*, 3442-3445.

89. Lee, D. W.; Hong, T.-K.; Kang, D.; Lee, J.; Heo, M.; Kim, J. Y.; Kim, B.-S.; Shin, H. S., Highly controllable transparent and conducting thin films using layer-by-layer assembly of oppositely charged reduced graphene oxides. *J. Mater. Chem.* **2011**, *21*, 3438-3442.

90. Hwang, H.; Joo, P.; Kang, M. S.; Ahn, G.; Han, J. T.; Kim, B.-S.; Cho, J. H., Highly Tunable Charge Transport in Layer-by-Layer Assembled Graphene Transistors. *ACS Nano* **2012**, *6*, 2432-2440.

91. Yang, S. H.; Lee, T.; Seo, E.; Ko, E. H.; Choi, I. S.; Kim, B.-S., Interfacing Living Yeast Cells with Graphene Oxide Nanosheets. *Macromol. Biosci.* **2012**, *12*, 61-66.

92. Montilla, F.; Cotarelo, M. A.; Morallon, E., Hybrid sol-gel-conducting polymer synthesised by electrochemical insertion: tailoring the capacitance of polyaniline. *J. Mater. Chem.* **2009**, *19*, 305-310.

93. Lee, S. W.; Yabuuchi, N.; Gallant, B. M.; Chen, S.; Kim, B.-S.; Hammond, P. T.; Shao-Horn, Y., High-power lithium batteries from functionalized carbon-nanotube electrodes. *Nat. Nanotechnol.* **2010**, *5*, 531-537.

94. Wang, Y. G.; Li, H. Q.; Xia, Y. Y., Ordered Whiskerlike Polyaniline Grown on the Surface of Mesoporous Carbon and Its Electrochemical Capacitance Performance. *Adv. Mater.* **2006**, *18*, 2619-2623.

95. Zhang, H.; Cao, G.; Wang, Z.; Yang, Y.; Shi, Z.; Gu, Z., Tube-covering-tube nanostructured polyaniline/carbon nanotube array composite electrode with high capacitance and superior rate performance as well as good cycling stability. *Electrochem. Commun.* **2008**, *10*, 1056-1059.

PART II. Ionic Liquid Modified Graphene Nanosheets Anchoring Manganese Oxide Nanoparticles as Efficient Electrocatalysts for Zn-air Batteries

I. INTRODUCTION

The limited availability of fossil fuel and environmental impacts has stimulated intense research on alternative energy storage and conversion systems. Electrochemical energy storage and conversion technologies are of vital importance to enable effective utilization of renewable energy sources and the creation of sustainable electric transportation. Recently, rechargeable lithium-ion (Li-ion) batteries have been significantly considered and developed to accommodate increasing energy demands for emerging applications in energy storage in smart grids and electrified transportations.¹ However, conventional Li-ion batteries cannot sufficiently satisfy the long-term energy storage requirements, because of their inherent gravimetric energy limitation associated with Li intercalation.²⁻⁴ Thus, current Li-ion batteries have limited for the practical application of emerging applications.

To overcome these limitations, one promising approach is to employ four-electron redox reaction of oxygen, where metal-air batteries have recently shown the potential to provide much higher gravimetric energy density, that of conventional Li-ion batteries (150~200 Wh/kg), as shown in **Figure 11**.⁵⁻¹⁰ Metal-air batteries generate electricity through an electrochemical redox reaction between metal and oxygen in air. The most prominent feature of a metal-air battery is the combination of a metal anode with high energy density and an air electrode with open cell structure to readily access the oxygen as cathode active materials continuously and almost infinitely from air. In addition, they exhibit notable advantages such as low cost, relatively high capacity, facile nature of handling and processing, and environmental benignity.¹¹⁻¹⁵ Therefore, metal-air batteries have received much attention as a possible alternative and promising power sources for applications in next-generation electronics, electrified transportations and energy storage of smart grids.

Herein, we present a simple approach of integrating manganese oxide nanoparticles into electrically conductive graphene sheets *via* a solution-based growth mechanism to afford hybrid graphene/Mn₃O₄ nanoparticles. Furthermore, we investigated their potential as an efficient electrocatalyst for the ORR in a Zn-air battery. In this study, we introduced the ionic liquid moiety onto the surface of graphene oxide with the aim of introducing the manganese oxide precursor on the surface of graphene as well as benefiting from the many features of the ionic liquid moiety (i.e. high ion conductivity, wide electrochemical windows, and the low interfacial energy between the graphene and the nanoparticles) that play a key role in enhancing the electrochemical activity of the resulting hybrid nanostructure.

1.1 Introduction of Zn-air batteries

Because of the remarkably high theoretical energy density compared with other conventional

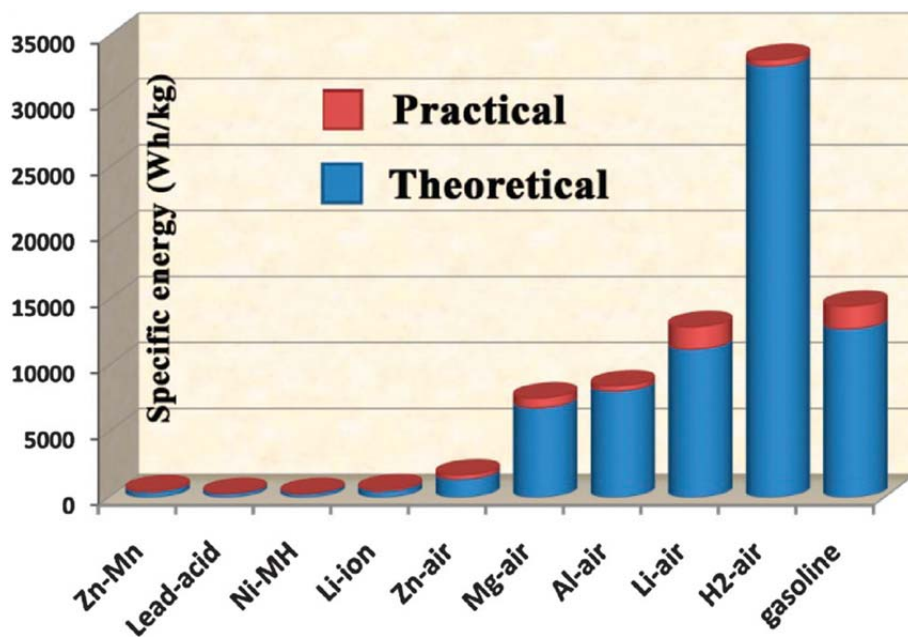
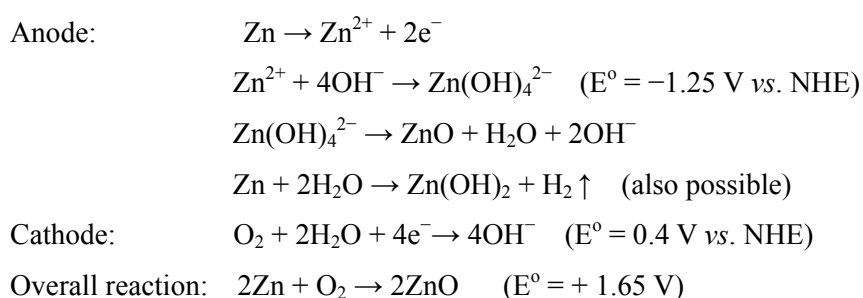


Figure 11. Comparison of the gravimetric energy density of some representative types of primary/rechargeable batteries, metal–air batteries, H₂–air fuel cell and gasoline. The theoretical values are calculated on the basis of thermodynamics of active materials.¹⁶

batteries such as the primary Zn–MnO₂ (Zn–Mn) and the rechargeable lead–acid, nickel–metal hydride (Ni–MH) and lithium–ion batteries,¹⁷ metal–air batteries represent one class of promising electrochemical systems for applications in next-generation electronics, hybrid electric transportations, and energy storage of smart grids.

Metal–air batteries are composed of three parts; pure metal such as magnesium (Mg), aluminum (Al), iron (Fe), lithium (Li) and zinc (Zn) as an anode material, an air–electrode with high porosity as the cathode, and a separator soaked in electrolyte (**Figure 12**). Among the diverse metal–air batteries, Zn–air batteries in particular have much attention for aqueous system due to their unique advantages such as low cost, abundance, low equilibrium potential, environmental benignity, and good safety.^{11, 12, 18} The Al– and Fe–metal can be more easily corroded than Zn in alkaline solution, although they have a much higher energy density than Zn–air batteries (1084 Wh/kg).¹⁹ Li–metal is explosively reactive with water, thus it is not suitable for aqueous system, despite their extremely high theoretical specific energy density (11,700 Wh/kg).

In Zn–air batteries, the zinc metal anode is oxidized and releases electrons to the external circuit when the cell is discharged (**Figure 13**). Simultaneously, oxygen diffused into the air-cathode, accepts the electrons from the anode and is reduced to oxygen-containing species (oxygen reduction reaction, ORR). The dissociated metal ions and oxygen-reduced species transferred across the electrolyte and combine to form a by-product of metal oxides; this overall procedure during discharge can be described as the following electrochemical reactions of anode and cathode in alkaline solution, respectively.



When the cell is charged, the process is reversed, with metal plating at the anode and oxygen evolving at the cathode (oxygen evolution reaction, OER). Because the solubility of oxygen is generally low in aqueous electrolyte and an electrocatalyst is required to facilitate its redox reactions, the cathode electrochemical reactions mainly take place at the liquid-gas-solid interface, also called three phase reaction, in the air electrode. Hence, oxygen transportation properties of the electrolyte play important roles in determining the battery performance.^{20, 21}

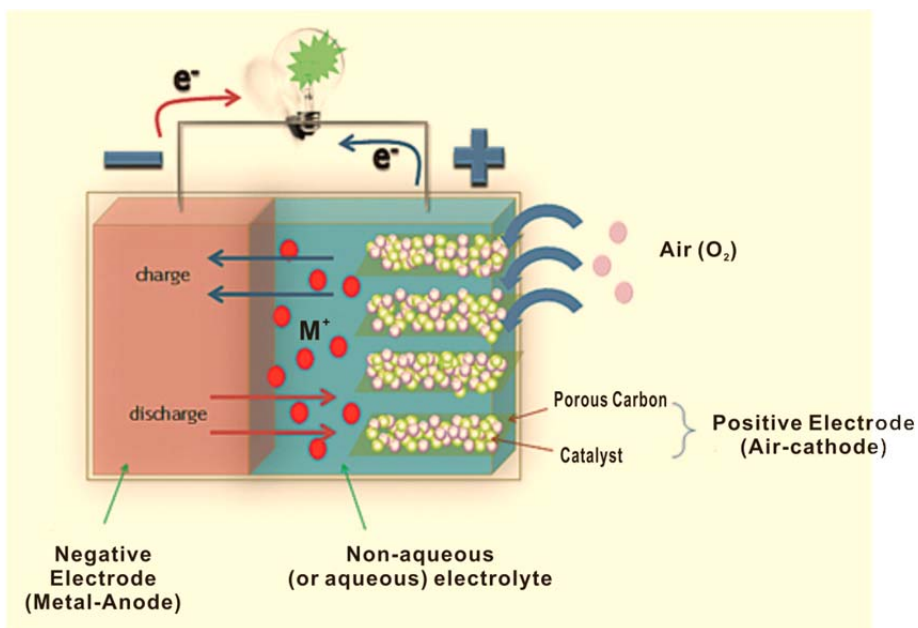


Figure 12. Schematic representation of the structure and operation principle of a metal-air battery.

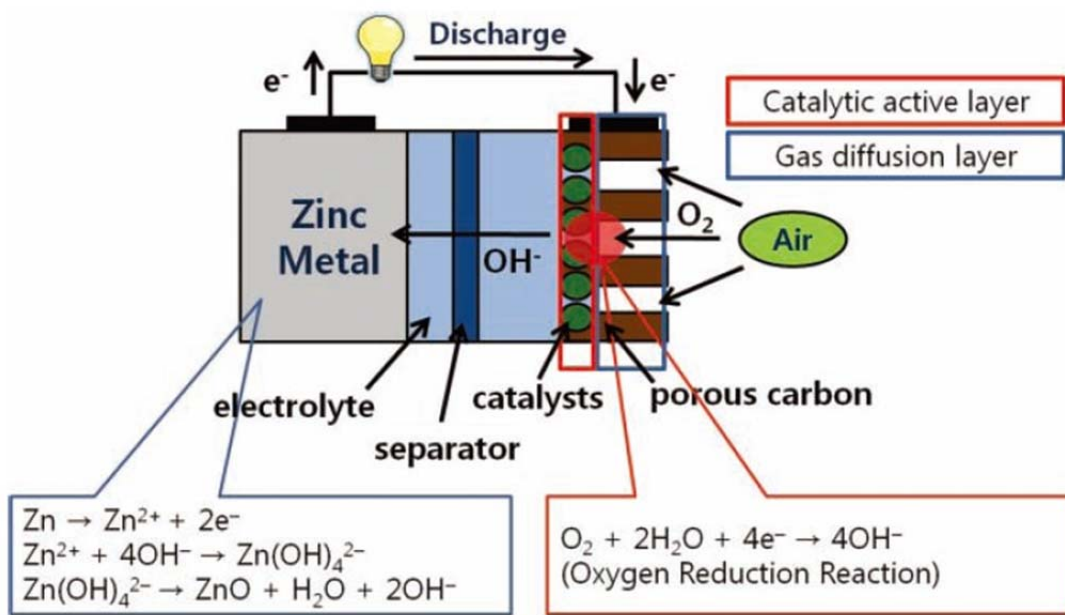


Figure 13. Working principle and each electrode reaction of zinc-air battery. Note the red circle where three phase reaction (oxygen (gas), catalysts (solid) and electrolyte (liquid)) occur in air cathode.²²

1.2 Catalytic materials for air electrode

Despite their superior features, the metal-air batteries have limited the practical applications in various electric fields, because of the sluggish kinetics and irreversible electrochemical redox reaction in the air-electrode.²³ Typically, the rate of cathodic oxygen reduction reaction (ORR) is slower than that of metal oxidation in the anode that phenomenon conversely decreases power density and energy conversion efficiency. Thus, the activity of electrocatalysts for the cathodic oxygen reduction reaction (ORR) plays a vital role in determining the electrochemical performance of fuel-cells and metal-air batteries.

In general, the ORR can proceed in two different pathways: (1) a two-electron reduction with the formation of H_2O_2 as the intermediate; (2) a more efficient four-electron reduction to directly produce H_2O as the final product. Noble metals such as the platinum (Pt) and palladium (Pd) nanoparticles have been intensively studied as ORR catalysts, because of their superior catalytic activity, relatively low overpotential and high stability.²⁴⁻²⁸ As shown in **Figure 14**, the plot of volcano relationship for a series of diverse electrocatalyst based on the computational and experimental results have further indicated that noble metal catalysts display high catalytic activity and oxygen binding affinity.²⁹⁻³¹ However, the high price and scarcity of platinum necessitates either an increase in the efficiency of noble metal use or the exploitation of non-precious electrocatalysts. In addition, they induced some side effects such as intermediate tolerance, anode crossover, and sluggish kinetics hindered for practical applications.

Among noble-metal-free alternatives, manganese oxides have received intensive attention because of their high element abundance, low cost, lower environmental impact, and moderate activity. Besides, it can come in a variety of MnO_x forms such as γ - $MnOOH$, α - Mn_2O_3 , α - MnO_2 , birnessite- MnO_2 , and β - MnO_2 , which have all been identified as high performing catalysts.³²⁻³⁷ Because of high activity of MnO_x for peroxide disproportionation reaction, it is possible for MnO_x to catalyze 4-electron reduction of oxygen in combination with another material active for 2-electron reduction of oxygen to peroxide. The most prominent feature of a MnO_x catalyst is that it can serve in catalytic oxygen evolution reactions (OER), thus making them attractive as bifunctional catalysts for oxygen electrochemistry.

Carbon electrodes, the most common supports for the ORR catalysts in cathodes of metal-air batteries, have long been recognized as materials with high intrinsic activity for the electrochemical oxygen reduction process. Among carbon materials, graphene, a monolayer of aromatic carbon lattice, has recently drawn a tremendous amount of interest for ORR catalysis because of its extraordinary electrical, optical, thermal, and mechanical properties, which are greatly favorable for the harsh ORR process. Taking full advantage of its chemical stability and high conductivity along with its high specific surface area, the graphene nanosheet is an excellent substrate for hosting and growing functional nanomaterials for high-performance electrochemical and electrocatalytic devices.³⁸⁻⁴⁰

1.3 Exploration the ORR kinetics of catalysts based on the Koutecky-Levich equation

To explore the ORR and the related kinetics, we used the Koutecky–Levich (K-L) equation transformed the obtained rotating-disk electrode (RDE) experiments. The linearity of the Koutecky-Levich plots and near parallelism of the fitting lines suggests first-order reaction kinetics toward the concentration of dissolved oxygen and similar electron transfer numbers for ORR at different potentials.⁴¹

$$\frac{1}{i} = \frac{1}{i_k} + \frac{1}{i_{dl}} = \frac{1}{i_k} + \frac{1}{B\omega^{0.5}} \quad (1)$$

$$i_k = nFAkC_{O_2} \quad (\text{kinetic current}) \quad (2)$$

$$i_{dl} = 0.20nFAC_{O_2}D_{O_2}^{2/3}\nu^{-1/6}\omega^{1/2} \quad (\text{diffusion limiting current}) \quad (3)$$

where i_k represents the kinetic current; i_{dl} is the diffusion limiting current; n is the number of electrons transferred per O_2 molecule; F is the Faraday constant (96485 C/mol); A is the geometric area of the disk electrode ($7.06 \times 10^{-6} \text{ m}^2$); k (m/s) is the rate constant for the ORR; C_{O_2} is the saturated concentration of O_2 in solution (1.21 mol/m^3 in 0.10 M KOH); ν is the kinematic viscosity ($1 \times 10^{-6} \text{ m}^2/\text{s}$ in 0.10 M KOH); D_{O_2} is the diffusion coefficient of O_2 in solution ($1.87 \times 10^{-9} \text{ m}^2/\text{s}$ in 0.10 M KOH); and ω is the angular frequency of the rotation (rad/s). From the linear relationship between i^{-1} vs. $\omega^{-0.5}$ based on the Koutecky–Levich equation, we can obtain the number of electrons transferred (n) from the slope and compare the kinetic current (i_k) from the intercept.

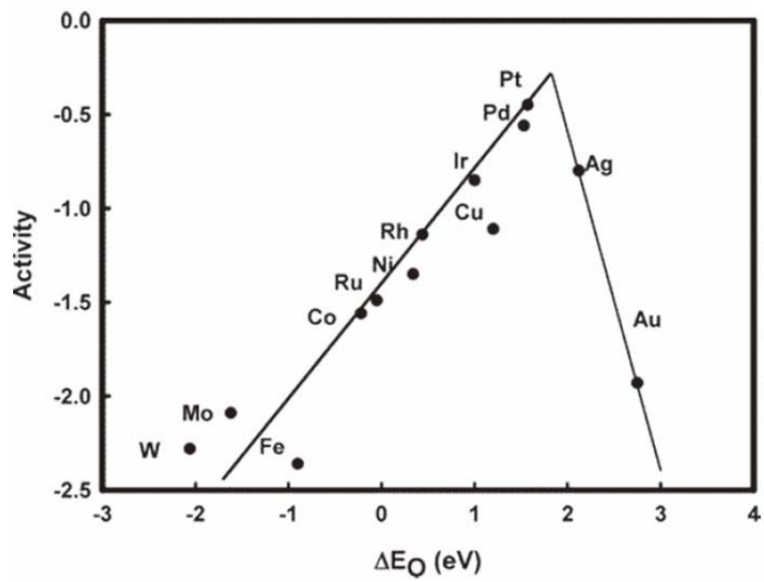


Figure 14. Trends in oxygen reduction activity (defined in the text) plotted as a function of the oxygen binding energy.³⁰

II. EXPERIMENT

2.1 Procedures of graphene oxide (GO) nanosheets

Graphite oxide was synthesized from graphite (Aldrich, <20 μm) by modified Hummers method and exfoliated to give a stable, brown dispersion of graphene oxide (GO, typically conc. of 0.50 mg/mL) under ultrasonication for 40 min and then centrifuged at 4000 rpm for 10 min to remove any aggregates remained in the suspension.

2.2 Preparation of ionic liquid moiety (IL-NH₂)

In the typical procedure according to the literature,⁴² 3-bromo-propylamine hydrobromide (1.1 g, 5.0 mmol) and 1-methyl-imidazole (0.395 mL, 5.0 mmol) were added to 15 mL ethanol, forming a colorless solution which was refluxed under nitrogen for 24 h. The resulting turbid mixture was purified by re-crystallization from ethanol, with ethyl acetate as an anti-solvent. Finally, the resulting white powder was dried under vacuum at 60 °C overnight and then purified.

2.3 Preparation of ionic liquid modified graphene oxide nanosheet (GO-IL) and reduced graphene oxide nanosheet (rGO-IL)

Ionic liquid modified GO nanosheets (GO-IL) were prepared by reacting GO with excess IL-NH₂ (conc. 0.50 mg/mL) under stirring for 5 h in the presence of *N*-ethyl-*N'*-(3-dimethyl aminopropyl) carbodiimide methiodide (EDC, 98%, Alfa Aesar). The resulting suspension was dialyzed (MWCO 12000–14000, SpectraPore) for a few days to remove any by product and residuals during functionalization. The prepared GO-IL suspensions exhibited a fairly good colloidal stability over a wide span of pH conditions. Chemical reduction of the GO-IL to rGO-IL was carried out by adding hydrazine as reported previously.

2.4 Preparation of catalyst ink for rotating disk electrode

Catalyst ink was prepared by ultrasonically mixing 2.0 mg of as-prepared sample with 1.0 mL of pure deionized water for 1 h in order to make homogeneous suspension. Then, 3 μL of the prepared catalytic ink was transferred to the surface of 3 mm diameter glassy carbon electrode using a micropipette. Finally, the ink was dried for 10 min under vacuum conditions at room temperature to form a thin catalyst film on the glassy carbon electrode as a working electrode.

2.5 Rotating disk electrode (RDE) experiments

All half-cell experiments for the ORR using rotating disk electrode (RDE) (ALS Co., Ltd) were carried out under same conditions where Pt wire and Hg/HgO were used as a counter and a reference electrode, respectively; 0.10 M KOH is used as an electrolyte; pure oxygen gas (99.9%) was purged for 30 min before each RDE experiment to make an electrolyte oxygen saturated condition. Rotation

speeds were changed in this RDE measurement to deduce kinetic parameters related to ORR to construct the Koutecky–Levich plot. Electrochemical characterization of as-prepared catalysts were conducted using a single potentiostat (Ivium) with a scan rate is 10 mV/s and potential range from 0.15 V to -0.7 V.

2.6 Preparation of air electrode

All air electrodes used in this Zn–air full cell test are prepared with fixed weight composition; activated carbon (Darco G-60A, Sigma-Aldrich) is 62 wt% + poly-tetrafluoroethylene (PTFE) binder 30 wt% (60 wt% PTFE emulsion in water, Sigma-Aldrich) + as-prepared catalysts is 8 wt%. After sonicating each material in DI-water for 1 h, each suspension was then mixed ultrasonically for 1 h to form a homogeneous suspension. The excess water is removed by filtering the homogeneous suspension and then the slurry is dried at 60 °C. By adding isopropyl alcohol to dried black powder, air electrodes were manufactured *via* a kneading and rolling process to make the desired thickness of air cathode. Finally, Ni-form as a current collector was attached to the back side of the air electrode. The thickness of all air cathodes was set to 600 μm to minimize the thickness factor of electrode to overall cell performance.

2.7 Zinc air full cell assembly

For the Zinc-air full cell test, homemade Zn-air single cell were used in this experiments. 1 g of zinc powder (Umicore) was used as anode electrode. Nylon net filter (Millipore) was used as a separator. A 16-pi air electrode is used as cathode electrode. The galvanodynamic experiment is carried out with a multichannel potentiostat (WBCS 3000, WonA Tech, Korea) with various current densities from 0 to 200 mA/cm^2 to characterize the Zn-air single cell performance.

III. RESULTS AND DISCUSSION

3.1 Ionic liquid (IL) modified graphene nanosheets

Highly stable and homogeneous GO suspension was prepared by following the modified Hummers method.⁴³⁻⁴⁵ To afford the ionic liquid (IL) moiety functionalized GO (GO-IL), 1-(3-aminopropyl)-3-methylimidazolium bromide was reacted with the carboxylic acid groups on surface of graphene nanosheets through the *N*-ethyl-*N'*-(3-dimethyl aminopropyl)carbodiimide methiodide (EDC) mediated reaction (**Scheme 2**). The successful functionalization of GO with the IL moiety was confirmed by zeta-potential measurements, which indicates a surface charge conversion from -52.0 mV to $+45.2$ mV upon functionalization. In addition, high-resolution X-ray photoelectron spectroscopy (XPS) further supported the presence of an IL moiety on the graphene nanosheets with two characteristic peaks at 399.3 and 401.9 eV, corresponding to the imidazolium ring of ionic liquid (**Figure 15**). As noted in other literature, the presence of the IL moiety would enhance the solubility of graphene in a wide range of solvents, facilitate its electrocatalytic activity and enhance its conductivity, hence improving overall the performance of the electrocatalyst.

3.2 rGO-IL/Mn₃O₄ nanocomposites for electrocatalysts

We carried out a chemical reduction by reducing agent, hydrazine, to render the restoration for electrical and structural properties of GO-IL. Then, manganese oxide nanoparticles were grown onto the as-prepared reduced GO-IL (rGO-IL) nanosheets by a simple hydrolysis reaction with the manganese precursor, NaMnO₄, in aqueous solution (**Scheme 2**). Specifically, the manganese precursor was mixed through the electrostatic interactions in various feeding ratios (the ratio of rGO-IL to Mn precursor ranges from 1 to 20), followed by heating at 85 °C for 1 h. The resulting rGO-IL/Mn₃O₄ composite was filtered and washed thoroughly with deionized water and dried in the oven at 50 °C.

3.3 Characterizations of rGO-IL/Mn₃O₄ nanocomposites electrocatalysts

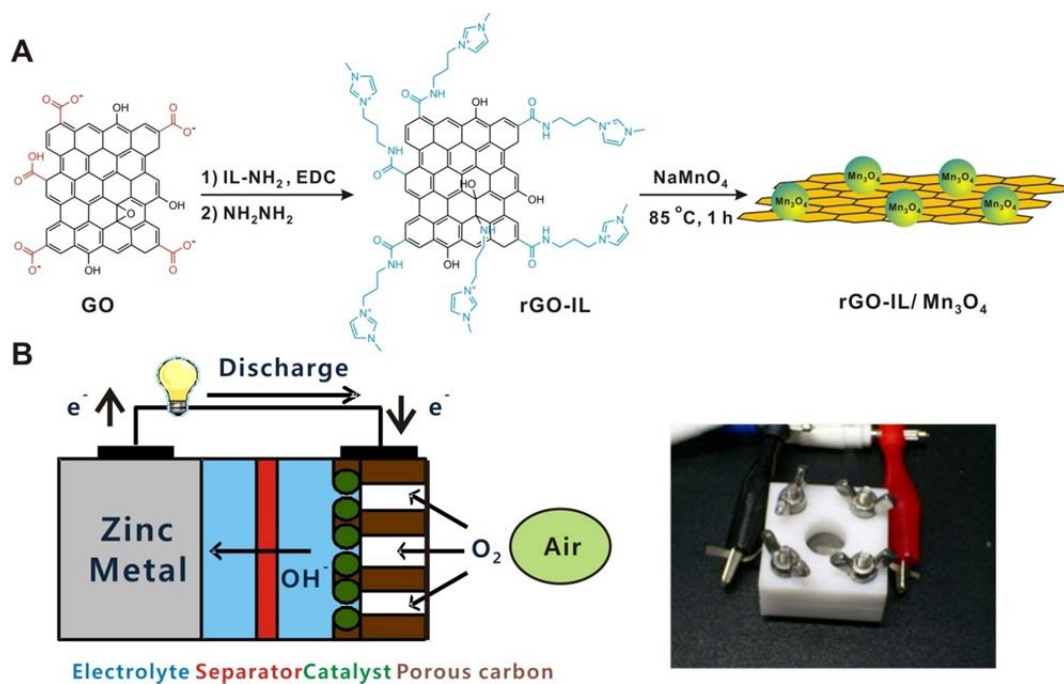
The crystalline structure of the rGO-IL/Mn₃O₄ nanocomposites was examined by X-ray diffraction (XRD) patterns as shown in **Figure 16**, which results indicate a good agreement with hausmannite-Mn₃O₄ diffraction pattern (JCPDS #80-0382). The morphological structures of the rGO-IL/Mn₃O₄ nanocomposites were characterized by scanning electron microscopy (SEM) and high-resolution transmission electron microscopy (HR-TEM). Based on the SEM and TEM images in **Figure 17**, we confirmed the partially poor-distribution of Mn₃O₄ nanoparticles on the surface of graphene sheets possessing relatively spherical morphology with an average diameter of 9.45 ± 1.72 nm. HRTEM images further reveal that crystal lattice fringes throughout the entire nanoparticles formed on the graphene sheet that matched with the major peaks of crystalline Mn₃O₄ nanoparticles, which is well-consistent with XRD results. Further the energy dispersive spectroscopy (EDS) elemental mapping

analysis of hybrid rGO–IL/Mn₃O₄, we observed the presence of the rGO–IL nanosheets by distinctive elements such as C, O and N as well as the presence of Mn₃O₄ nanoparticles by Mn and O elements (**Figure 17f**). Given the rather non-uniformly distributed Mn₃O₄ nanoparticles on the surface of rGO–IL, we postulate that the ionic linkage between the surface of rGO–IL and the manganese precursor are possibly not uniformly distributed on the surface of graphene nanosheets. The graphene–nanoparticle interaction, however, allows good dispersion of Mn₃O₄ nanoparticles grown on the rGO nanosheets thus avoiding the potential aggregation of nanoparticles during the electrocatalytic cycles.

3.4 Electrocatalytic activities of hybrid catalysts

To assess the electrocatalytic activities of hybrid electrocatalysts, the rotating-disk electrode (RDE) experiments were conducted in O₂ saturated 0.1 M KOH aqueous solution with wide span of rotating rates from 900 to 3200 rpm. Since the electrons resulting from the oxidation of zinc metal should flow efficiently to the nanoparticle-supporting carbon substrate to reduce the oxygen during the actual operation of a Zn–air battery, the electrical conductivity together with the catalytic activity of the nanoparticles are critical factors in designing and developing the efficient catalyst. Therefore, we employed two independent strategies to gain the insight on the catalytic activity: 1) chemical attachment of the ionic liquid moiety as well as chemical reduction of the graphene sheet to increase the conductivity of the system and electrocatalytic activity and 2) tuning the ratio of the Mn precursor with respect to the rGO–IL to determine the optimum ratio of our hybrid rGO–IL/Mn₃O₄ catalyst for enhanced ORR activity while preserving necessary electrical conductivity.

As shown in the **Figure 18**, covalent attachment of the ionic liquid moiety onto the graphene nanosheet results in a higher limiting current and more positive onset potential than that of a plain, unmodified GO. This is consistent with the previous reports that the presence of the ionic liquid moiety would facilitate the electrocatalytic activity between the metal and oxygen,⁴⁶ as well as increase the solubility of the oxygen which can affect the enhanced reduction rate of oxygen to perhydroxyl or hydroxyl ions.^{47, 48} Moreover, the chemically reduced graphene oxide (rGO–IL) has both a higher limiting current and more positive onset potential than GO–IL. Taken together, these data clearly support the critical role of the ionic liquid moiety as well as the enhanced conductivity gained upon the chemical reduction process of the GO nanosheet. Although electrical conductivity is another factor in determining ORR activity, the actual ORR activity of carbon materials is not sufficient to reduce oxygen effectively. When comparing the rGO–IL with rGO–IL/Mn₃O₄ composites, the latter has a higher ORR activity as expected, among which rGO–IL/Mn₃O₄ (10 : 1) has the highest catalytic activity. These results clearly show that Mn₃O₄ nanoparticles facilitate the reaction effectively; however, higher Mn₃O₄ contents (rGO–IL/Mn₃O₄ (2 : 1), 52.5% Mn content as determined from TGA) can reduce ORR activity compared with a lower content of Mn₃O₄ (rGO–IL/Mn₃O₄ (10 : 1), 19.2% Mn content) (**Figure 19**). We postulate that the relatively larger content of



Scheme 2. (a) Schematic representation of the functionalization of the surface of graphene oxide and subsequent formation of nanoparticles. (b) Cartoon of Zn-air battery cell with a photograph of the actual cell tested.

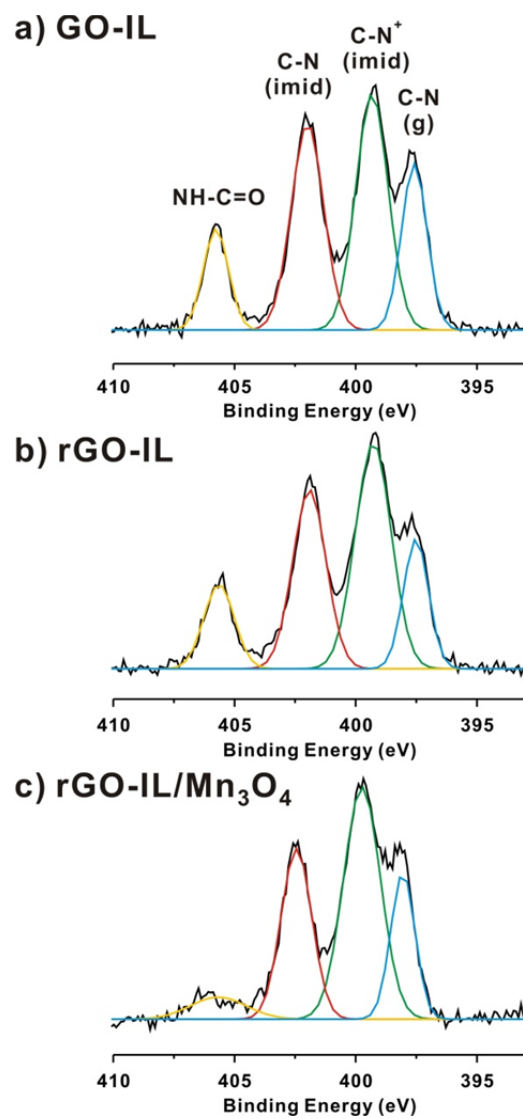


Figure 15. Deconvoluted high-resolution N1s XPS spectra of samples in this study. (a) GO, (b) rGO-IL, and (c) rGO-IL/Mn₃O₄ (10:1).

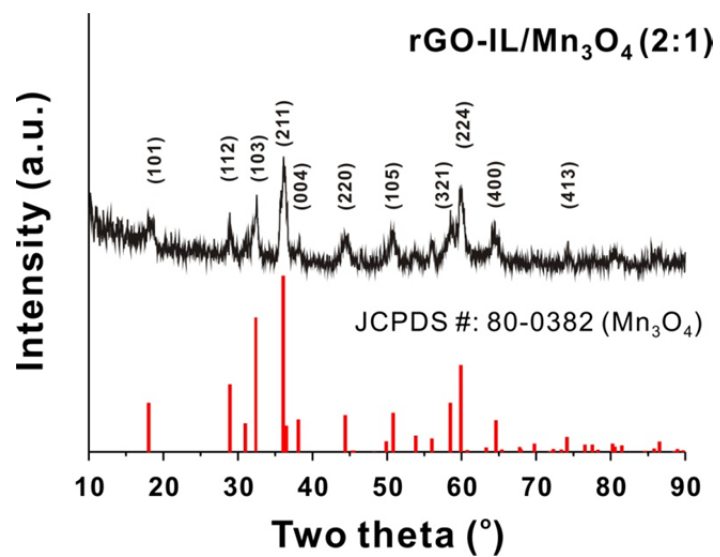


Figure 16. X-ray diffraction pattern of prepared hybrid rGO-IL/Mn₃O₄ (2:1) with the reference Mn₃O₄ diffraction pattern.

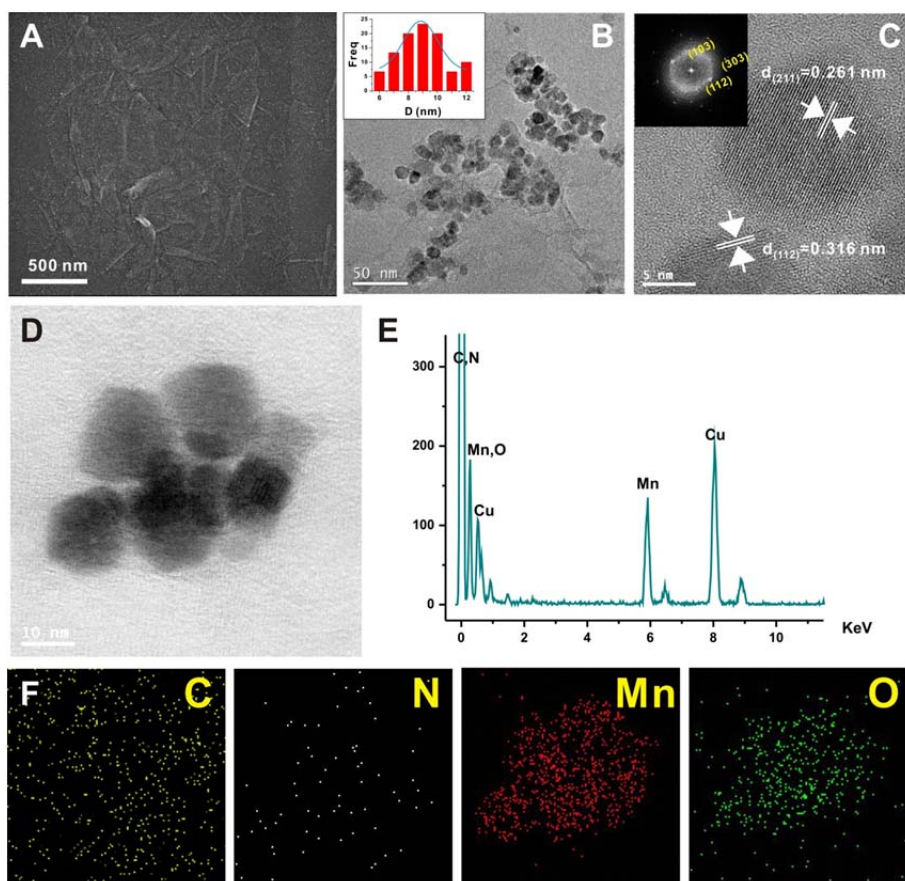


Figure 17. (a) SEM and (b) TEM images of rGO-IL/Mn₃O₄ composites with size-distribution of Mn₃O₄ nanoparticles. (c) HR-TEM image of Mn₃O₄ nanoparticles with the inset of the corresponding SAED pattern and (d, e, f) STEM and the EDX elemental mapping image of hybrid rGO-IL/Mn₃O₄ (10:1) composites.

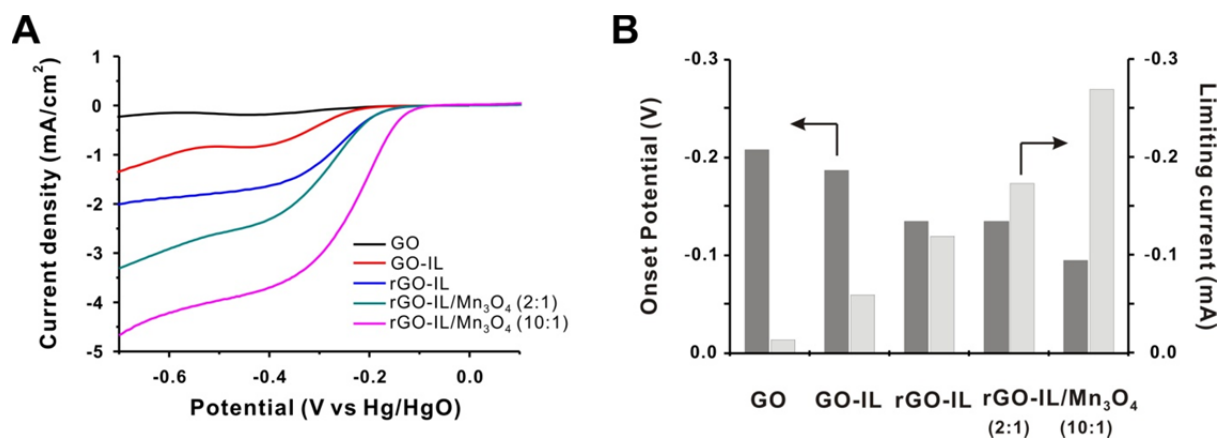


Figure 18. Rotating disk electrode (RDE) experiments of various samples prepared in this study. (a) half-cell data and (b) comparison of onset potential and limiting current of each sample of GO, GO-IL, rGO-IL, rGO-IL/Mn₃O₄ (2:1), and rGO-IL/Mn₃O₄ (10:1). The rotation rate is 3200 rpm and the scan rate is 10 mV/s; 0.10 M KOH is used as an electrolyte. Pt wire and Hg/HgO is used as a counter and reference electrode with a 3-mm² diameter working electrode, respectively. Onset potential was measured at -0.002 mA/cm² and limiting current was measured at -0.45 V.

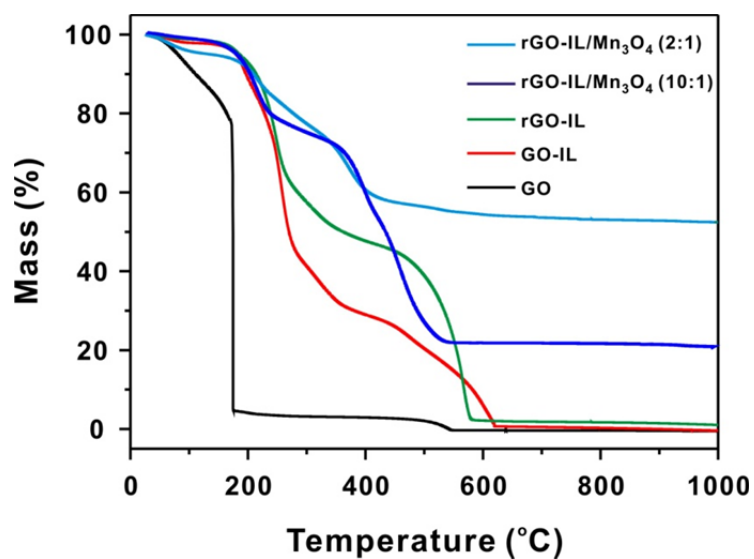


Figure 19. TGA thermograms of all samples used in this study. rGO-IL/Mn₃O₄ (2:1) and rGO-IL/Mn₃O₄ (10:1) show the relative percentage of Mn₃O₄ within the composite is 52.5% and 19.2%, respectively. The thermograms were obtained at a scan rate of 10 °C/min under air.

Mn₃O₄ with respect to the graphene sheet results in a lower electrical conductivity, which in turn, has an adverse effect on the ORR activity. It is also of note that the absolute amount of Mn₃O₄ in the hybrid is not the major factor in governing the ORR activity, since the limiting current normalized to the effective mass of active Mn₃O₄ within the hybrid rGO–IL/Mn₃O₄ yields approximately 4 times higher mass activity for the rGO–IL/Mn₃O₄ (10 : 1) sample (–233.9 mA/mg,Mn at –0.45 V) than that of rGO–IL/Mn₃O₄ (2 : 1) (–55.2 mA/mg,Mn at –0.45 V).

Given the RDE data, we calculated the average number of electrons transferred from the samples of two different Mn₃O₄ contents based on the K-L plots (**Figure 20**), particularly rGO–IL/Mn₃O₄ (2 : 1) and (10 : 1). To our surprise, we found that the average number of transferred electrons (n) of rGO–IL/Mn₃O₄ (2 : 1) is 2.75 while it increased to 3.50 in the case of rGO–IL/Mn₃O₄ (10 : 1). With these results, it is reasonable to estimate that there exist two independent mechanisms depending on the contents of Mn₃O₄ in the hybrid rGO–IL/Mn₃O₄ catalyst. Specifically, the corresponding number of electrons (3.50) for rGO–IL/Mn₃O₄ (10 : 1) indicates an efficient one-step, quasi-4-electron transfer similar to the commercial Pt/C catalyst. On the other hand, the electron transfer number (2.75) of rGO–IL/Mn₃O₄ (2 : 1) is close to the dominant two-step, 2-electron pathway, as is the case for many other carbon-based electrode materials (**Figure 21**). It is interesting to note that the reaction mechanism is tunable simply with the relative amount of nanoparticles supported onto the graphene sheets.

3.5 Zinc–air cell performance

Because the study on half-cell experiments such as RDE presents only the performance as a catalyst, we have to evaluate the actual ORR performance of catalysts in a Zn–air full cell. For that purpose, we have evaluated the electrochemical performance of a single Zn–air cell composed of an anode of zinc powder together with a hybrid rGO–IL/Mn₃O₄ electrocatalyst in the cathode electrode. *Via* a galvanodynamic method, the current density versus potential (reference to a Zn electrode) profile can be obtained under varying current density from 0 to 200 mA/cm² and one can calculate the maximum peak power density from a polarization curve for the Zn–air cell (**Figure 22**). As shown in the discharge profile of Zn–air full cell, the voltage difference in two cells of different Mn contents rises significantly with the increase of current density. This result indicates that a resistance effect on a Zn–air cell is more dominant when high current density is applied to the cell and also coincides with the fact that the oxygen reduction reaction becomes very sluggish due to a high overpotential. When the power density plot is constructed, similar trends between RDE and actual cell performance are observed and maximum peak power density of 120 mW/cm² can be obtained from the hybrid rGO–IL/Mn₃O₄ (10 : 1) sample. For comparison, identical procedures were applied to compare the efficiency of the air cathode with the commercial gas diffusion electrode (GDE) including MnOx (Meet Inc., Korea) and 20% Pt on Vulcan XC-72 (E-TEK). Although the 20% Pt/C exhibits the best

electrochemical performance among various samples, our hybrid rGO-IL/Mn₃O₄ (10 : 1) still illustrates better efficiency in the overall Zn-air fuel cell performance than the commercial air cathode under the current density from 0 to 200 mA/cm². With further improvements, we believe this hybrid catalyst could be used as a potential candidate in low-cost electrocatalysts for metal-air batteries and alkaline fuel cells. For more practical application of our hybrid catalyst in various electrocatalytic reactions, our next endeavor should be focused more on addressing the stability and durability, as well as the product cost of the modified graphene nanosheet and hybrid catalyst.

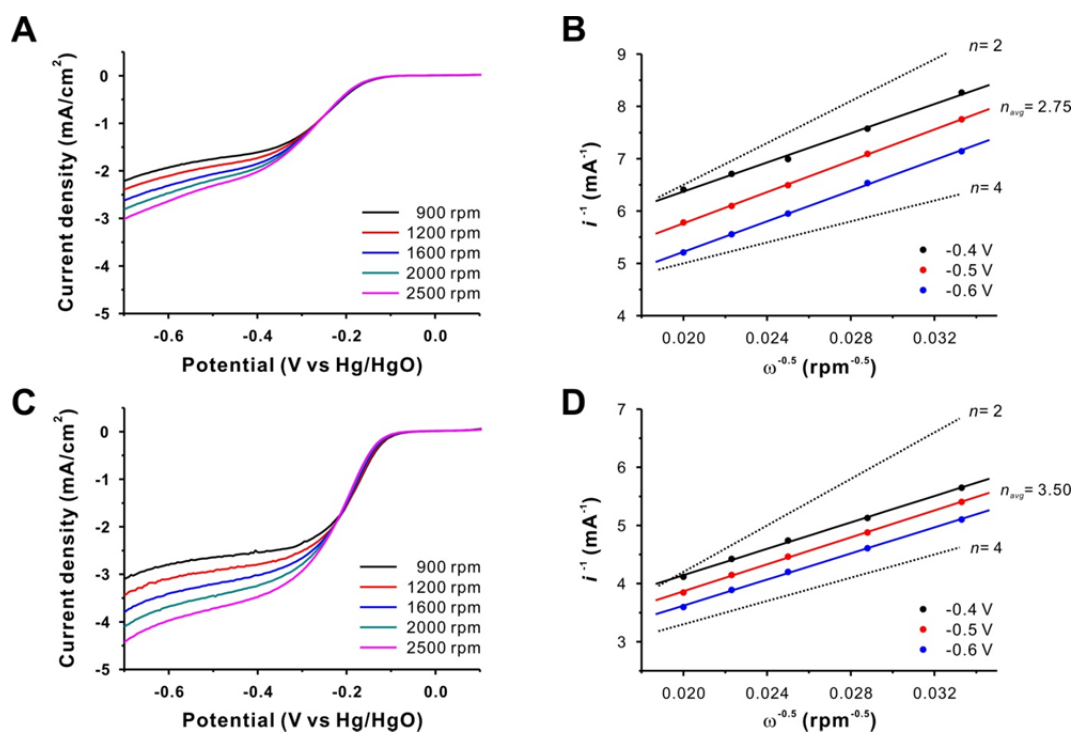


Figure 20. RDE experiments and the corresponding Koutecky-Levich plots of (a, b) rGO-IL/ Mn₃O₄ (2:1) and (c, d) rGO-IL/Mn₃O₄ (10:1). The experiments were conducted at a scan rate of 10 mV/s in an O₂-saturated 0.10 M KOH solution. Theoretical slopes for $n = 2$ and 4 are also constructed for comparison.

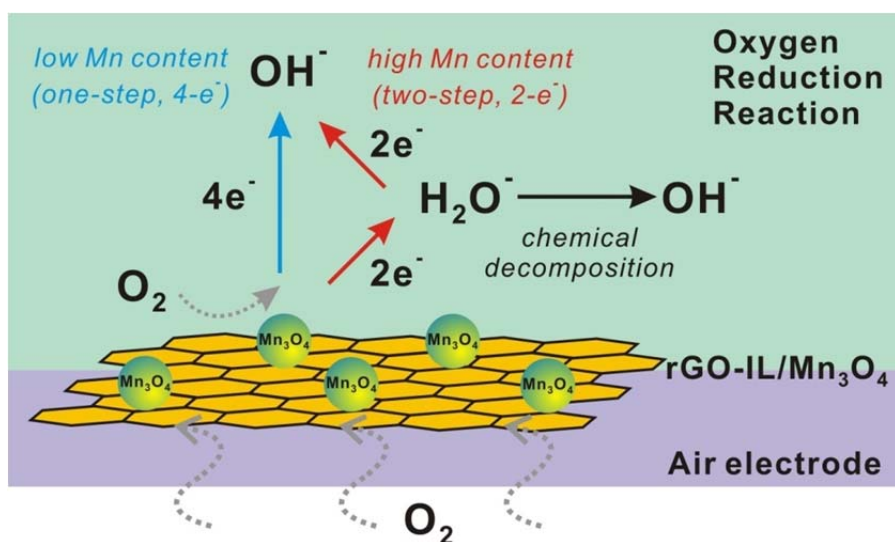


Figure 21. Schematic representation of the potential pathway of electrons during oxygen reduction reaction on the surface of rGO-IL/Mn₃O₄ electrocatalysts.

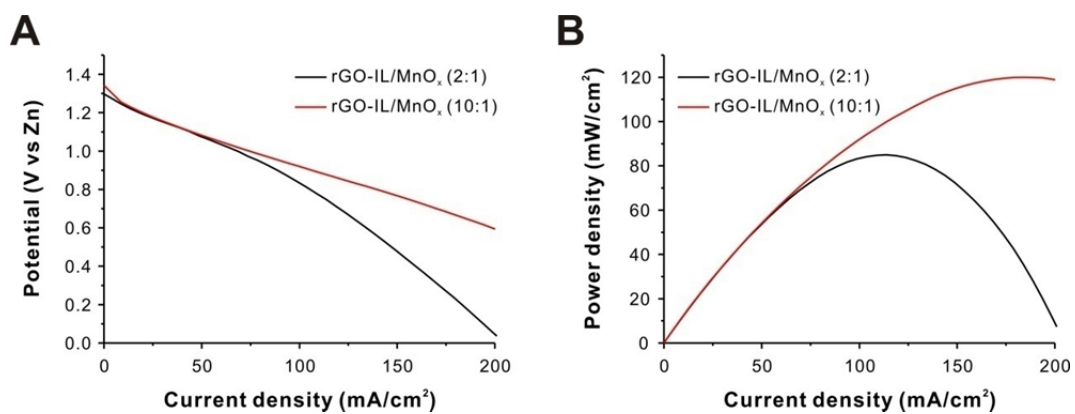


Figure 22. Single cell performance of zinc air battery assembled with hybrid rGO-IL/Mn₃O₄ electrocatalysts. (a) Polarization curve of zinc-air cell and (b) corresponding power density plot of (black) rGO-IL/Mn₃O₄ (2:1) and (red) rGO-IL/Mn₃O₄ (10:1) under the current density from 0 to 200 mA/cm².

IV. CONCLUSION

In summary, we present a simple and facile approach of integrating manganese oxide nanoparticles into the electrically conductive graphene sheets *via* a solution-based growth mechanism to afford hybrid graphene/Mn₃O₄ nanoparticles. The ionic liquid moiety on the graphene nanosheet was proven to be important in enhancing the electrocatalytic activity of the hybrid nanoparticles in oxygen reduction reaction with a one-step, quasi-4-electron transfer pathway. By utilizing the high activity of the graphene/Mn₃O₄ nanoparticles, we demonstrated their potential in the Zn–air battery, as they exhibit considerably high catalytic activity. By taking advantage of the facile synthetic nature of this hybrid nanoparticle with graphene nanosheet, we anticipate that the hybrid graphene/Mn₃O₄ nanoparticles will open new possibilities in applications as alternative low-cost catalysts for metal-air batteries and alkaline fuel cells.

REFERENCES

1. Owen, J. R., Rechargeable lithium batteries. *Chem. Soc. Rev.* **1997**, *26*, 259-267.
2. Whittingham, M. S., Lithium Batteries and Cathode Materials. *Chem. Rev.* **2004**, *104*, 4271-4302.
3. Arico, A. S.; Bruce, P.; Scrosati, B.; Tarascon, J.-M.; van Schalkwijk, W., Nanostructured materials for advanced energy conversion and storage devices. *Nat. Mater.* **2005**, *4*, 366-377.
4. Bruce, P. G.; Freunberger, S. A.; Hardwick, L. J.; Tarascon, J.-M., Li-O₂ and Li-S batteries with high energy storage. *Nat. Mater.* **2012**, *11*, 19-29.
5. Débart, A.; Paterson, A. J.; Bao, J.; Bruce, P. G., α -MnO₂ Nanowires: A Catalyst for the O₂ Electrode in Rechargeable Lithium Batteries. *Angew. Chem. Int. Ed.* **2008**, *47*, 4521-4524.
6. Lu, Y.-C.; Gasteiger, H. A.; Parent, M. C.; Chiloyan, V.; Shao-Horn, Y., The Influence of Catalysts on Discharge and Charge Voltages of Rechargeable Li-Oxygen Batteries. *Electrochem. Solid-State Lett.* **2010**, *13*, A69-A72.
7. Lu, Y.-C.; Gasteiger, H. A.; Shao-Horn, Y., Catalytic Activity Trends of Oxygen Reduction Reaction for Nonaqueous Li-Air Batteries. *J. Am. Chem. Soc.* **2011**, *133*, 19048-19051.
8. Lu, Y.-C.; Kwabi, D. G.; Yao, K. P. C.; Harding, J. R.; Zhou, J.; Zuin, L.; Shao-Horn, Y., The discharge rate capability of rechargeable Li-O₂ batteries. *Energy Environ. Sci.* **2011**, *4*, 2999-3007.
9. Scrosati, B.; Hassoun, J.; Sun, Y.-K., Lithium-ion batteries. A look into the future. *Energy Environ. Sci.* **2011**, *4*, 3287-3295.
10. Jung, H.-G.; Hassoun, J.; Park, J.-B.; Sun, Y.-K.; Scrosati, B., An improved high-performance lithium-air battery. *Nat. Chem.* **2012**, *4*, 579-585.
11. McLarnon, F. R.; Cairns, E. J., The Secondary Alkaline Zinc Electrode. *J. Electrochem. Soc.* **1991**, *138*, 645-656.
12. Arora, P.; Zhang, Z., Battery Separators. *Chem. Rev.* **2004**, *104*, 4419-4462.
13. Palacin, M. R., Recent advances in rechargeable battery materials: a chemist's perspective. *Chem. Soc. Rev.* **2009**, *38*, 2565-2575.
14. Li, X.; Zhu, A. L.; Qu, W.; Wang, H.; Hui, R.; Zhang, L.; Zhang, J., Magneli phase Ti₄O₇ electrode for oxygen reduction reaction and its implication for zinc-air rechargeable batteries. *Electrochim. Acta* **2010**, *55*, 5891-5898.
15. Yang, Z.; Zhang, J.; Kintner-Meyer, M. C. W.; Lu, X.; Choi, D.; Lemmon, J. P.; Liu, J., Electrochemical Energy Storage for Green Grid. *Chem. Rev.* **2011**, *111*, 3577-3613.
16. Cheng, F.; Chen, J., Metal-air batteries: from oxygen reduction electrochemistry to cathode catalysts. *Chem. Soc. Rev.* **2012**, *41*, 2172-2192.
17. Linden, D.; Reddy, T. B., Handbook of batteries. *New York* **2002**.
18. Neburchilov, V.; Wang, H.; Martin, J. J.; Qu, W., A review on air cathodes for zinc-air fuel cells. *J. Power Sources* **2010**, *195*, 1271-1291.

19. Sapkota, P.; Kim, H., Zinc–air fuel cell, a potential candidate for alternative energy. *J. Ind. Eng. Chem.* **2009**, *15*, 445-450.
20. Kowalczyk, I.; Read, J.; Salomon, M., Li-air batteries: A classic example of limitations owing to solubilities. *Pure Appl. Chem.* **2007**, *79*, 851-860.
21. McCloskey, B. D.; Bethune, D. S.; Shelby, R. M.; Girishkumar, G.; Luntz, A. C., Solvents' Critical Role in Nonaqueous Lithium–Oxygen Battery Electrochemistry. *J. Phys. Chem. Lett.* **2011**, *2*, 1161-1166.
22. Lee, J.-S.; Tai Kim, S.; Cao, R.; Choi, N.-S.; Liu, M.; Lee, K. T.; Cho, J., Metal–Air Batteries with High Energy Density: Li–Air versus Zn–Air. *Adv. Energy Mater.* **2011**, *1*, 34-50.
23. Kinoshita, K., *Electrochemical oxygen technology, the electrochemical society series*. Wiley, New York: 1992.
24. Zhang, J.; Vukmirovic, M. B.; Xu, Y.; Mavrikakis, M.; Adzic, R. R., Controlling the Catalytic Activity of Platinum-Monolayer Electrocatalysts for Oxygen Reduction with Different Substrates. *Angew. Chem. Int. Ed.* **2005**, *44*, 2132-2135.
25. Lim, B.; Jiang, M.; Camargo, P. H. C.; Cho, E. C.; Tao, J.; Lu, X.; Zhu, Y.; Xia, Y., Pd-Pt Bimetallic Nanodendrites with High Activity for Oxygen Reduction. *Science* **2009**, *324*, 1302-1305.
26. Yamamoto, K.; Imaoka, T.; Chun, W.-J.; Enoki, O.; Katoh, H.; Takenaga, M.; Sonoi, A., Size-specific catalytic activity of platinum clusters enhances oxygen reduction reactions. *Nat. Chem.* **2009**, *1*, 397-402.
27. Bing, Y.; Liu, H.; Zhang, L.; Ghosh, D.; Zhang, J., Nanostructured Pt-alloy electrocatalysts for PEM fuel cell oxygen reduction reaction. *Chem. Soc. Rev.* **2010**, *39*, 2184-2202.
28. Zhou, Z.-Y.; Tian, N.; Li, J.-T.; Broadwell, I.; Sun, S.-G., Nanomaterials of high surface energy with exceptional properties in catalysis and energy storage. *Chem. Soc. Rev.* **2011**, *40*, 4167-4185.
29. Hammer, B.; Norskov, J. K., Why gold is the noblest of all the metals. *Nature* **1995**, *376*, 238-240.
30. Nørskov, J. K.; Rossmeisl, J.; Logadottir, A.; Lindqvist, L.; Kitchin, J. R.; Bligaard, T.; Jónsson, H., Origin of the Overpotential for Oxygen Reduction at a Fuel-Cell Cathode. *J. Phys. Chem. B* **2004**, *108*, 17886-17892.
31. Santos, E.; Schmickler, W., d-Band Catalysis in Electrochemistry. *Chem. Phys. Chem.* **2006**, *7*, 2282-2285.
32. Post, J. E., Manganese oxide minerals: Crystal structures and economic and environmental significance. *Proc. Natl. Acad. Sci. USA* **1999**, *96*, 3447-3454.
33. Mao, L.; Arihara, K.; Sotomura, T.; Ohsaka, T., A novel electrochemical strategy for developing alkaline air electrodes by a combined use of dual functional catalysts. *Chem. Commun.* **2003**, 2818-2819.
34. Mao, L.; Zhang, D.; Sotomura, T.; Nakatsu, K.; Koshihara, N.; Ohsaka, T., Mechanistic study of

the reduction of oxygen in air electrode with manganese oxides as electrocatalysts. *Electrochim. Acta* **2003**, *48*, 1015-1021.

35. El-Deab, M. S.; Ohsaka, T., Manganese Oxide Nanoparticles Electrodeposited on Platinum Are Superior to Platinum for Oxygen Reduction. *Angew. Chem. Int. Ed.* **2006**, *45*, 5963-5966.

36. Lima, F. H. B.; Calegario, M. L.; Ticianelli, E. A., Electrocatalytic activity of manganese oxides prepared by thermal decomposition for oxygen reduction. *Electrochim. Acta* **2007**, *52*, 3732-3738.

37. Morozan, A.; Josselme, B.; Palacin, S., Low-platinum and platinum-free catalysts for the oxygen reduction reaction at fuel cell cathodes. *Energy Environ. Sci.* **2011**, *4*, 1238-1254.

38. Guo, S.; Wen, D.; Zhai, Y.; Dong, S.; Wang, E., Platinum Nanoparticle Ensemble-on-Graphene Hybrid Nanosheet: One-Pot, Rapid Synthesis, and Used as New Electrode Material for Electrochemical Sensing. *ACS Nano* **2010**, *4*, 3959-3968.

39. Wang, H.; Cui, L.-F.; Yang, Y.; Sanchez Casalongue, H.; Robinson, J. T.; Liang, Y.; Cui, Y.; Dai, H., Mn₃O₄-Graphene Hybrid as a High-Capacity Anode Material for Lithium Ion Batteries. *J. Am. Chem. Soc.* **2010**, *132*, 13978-13980.

40. Sun, Y.; Wu, Q.; Shi, G., Graphene based new energy materials. *Energy Environ. Sci.* **2011**, *4*, 1113-1132.

41. Treimer, S.; Tang, A.; Johnson, D. C., A Consideration of the Application of Koutecký-Levich Plots in the Diagnoses of Charge-Transfer Mechanisms at Rotated Disk Electrodes. *Electroanalysis* **2002**, *14*, 165-171.

42. Zhang, Y.; Shen, Y.; Yuan, J.; Han, D.; Wang, Z.; Zhang, Q.; Niu, L., Design and Synthesis of Multifunctional Materials Based on an Ionic-Liquid Backbone. *Angew. Chem. Int. Ed.* **2006**, *45*, 5867-5870.

43. Hummers, W. S.; Offeman, R. E., Preparation of Graphitic Oxide. *J. Am. Chem. Soc.* **1958**, *80*, 1339-1339.

44. Eda, G.; Fanchini, G.; Chhowalla, M., Large-area ultrathin films of reduced graphene oxide as a transparent and flexible electronic material. *Nat. Nanotechnol.* **2008**, *3*, 270-274.

45. Li, D.; Muller, M. B.; Gilje, S.; Kaner, R. B.; Wallace, G. G., Processable aqueous dispersions of graphene nanosheets. *Nat. Nanotechnol.* **2008**, *3*, 101-105.

46. Li, B.; Cao, H.; Shao, J.; Qu, M.; Warner, J. H., Superparamagnetic Fe₃O₄ nanocrystals@graphene composites for energy storage devices. *J. Mater. Chem.* **2011**, *21*, 5069-5075.

47. Snyder, J.; Fujita, T.; Chen, M. W.; Erlebacher, J., Oxygen reduction in nanoporous metal-ionic liquid composite electrocatalysts. *Nat. Mater.* **2010**, *9*, 904-907.

48. Wang, Z.; Latonen, R.-M.; Kvarnström, C.; Ivaska, A.; Niu, L., Preparation of Multi-Walled Carbon Nanotube/Amino-Terminated Ionic Liquid Arrays and Their Electrocatalysis towards Oxygen Reduction. *Materials* **2010**, *3*, 672-681.

ACKNOWLEDGEMENTS

UNIST라는 학교에 대학원 과정으로 진학을 하고 석사학위를 받고 졸업을 하기까지, 남들과는 달리 저에게 있어서는 결코 순탄치 않은 과정이었기에, 지금 받는 이 학위가 제 인생에 있어서 남다른 의미도 있고, 더불어 다음 단계로 한 발짝 나아가는데 있어서 좋은 밑거름이 되는 경험이었습니다.

먼저, 저에게 'Master'라는 자격증을 선사해주신 김병수 교수님께 감사 드리며, KBS그룹의 1호 대학원생이라는 명분아래 과분한 관심과 지도 그리고 좋은 연구의 기회를 열어주셔서 감사의 말씀을 드립니다. 앞으로도 좋은 연구지도 부탁드리며, 교수님께서 주신 가르침이 저희 후배들에게도 잘 전달될 수 있도록 노력하겠습니다.

그리고, 저의 연구에 많은 조언과 도움을 주신 송현곤 교수님, 이형일 교수님, 양성호 교수님께도 감사의 말씀을 드립니다.

그리고 언제나 뒤에서 든든하게 받쳐주고 있는 은용이형, 필재형. 묵묵히 자기 역할 잘 수행하는 유리, 잔소리 해도 꾸역꾸역 잘 들어주는 수은이, 그리고 내가 먼저 나가려고 했는데 이제 석사 디펜스부터 졸업식까지 봐야하는 은경이 & 은희.. ㅎㅎ 항상 뒤에서 받쳐주고 이끄는 대로 잘 따라와줘서 감사감사^^ 다들 부족한 저를 방장이라고 믿고 따라와줘서 고맙고, 잘했다는 생각은 안들지만 그래도 나 스스로는 열심히 했다고 생각하니, 공감하시면 마음속으로 박수라도 쳐주시면 좋겠네요 ㅎㅎ

그리고 이제 저의 박사과정 멘토가 되어 주실 정윤경 박사님.....ㅎ 앞으로도 좋은 조언 부탁드립니다, 기회가 된다면 함께 좋은 연구할 수 있으면 좋겠습니다.

마지막으로, 언제나 뒤에서 공부에만 집중할 수 있게끔 지원해주시고 응원해주는 우리 부모님께 감사의 말씀을 드리며, 이 글을 마칩니다.